14 Tests with prototypes

In this chapter we describe the most relevant results of the tests with detector prototypes, carried out during the past three years. Section 14.1 contains a brief description of the prototypes and of the data acquisition system. In Section 14.2 we present the results of tests with radioactive sources (^{55}Fe) and in Section 14.3 the results of tests in beam will be shown. In Section 14.4 we summarize the on-going activities and the plans for future test measurements.

14.1 Prototype description

Most of the results were obtained using a prototype Drift Chamber (DC) with dimensions identical to those anticipated for the final detector (see Chapter 4), except concerning the area, which is only 0.5×0.6 m^2. Chevron pad planes [1] with a pad area of 4.5 cm^2 are used for the readout. A sketch of the chevron geometry is presented in Fig. 14.1. The width of the pads is w=10 mm, the step (matching the anode wire pitch) is s=5 mm, and the overlap factor f_x=1.05. Nine chevron units (shaded area) are connected together to form a pad of 4.5 cm length. For mechanical stability, the pad plane thickness is 3.5 mm. The average capacitance of a pad is about 22 pF. Both the anode (W-Au, 25 μm diameter) and cathode wires (Cu-Be, 75 μm diameter) have a pitch of 5 mm and we use a staggered geometry. The drift region is 30 mm in length and the anode-cathode gap (h) is 3 mm. The entrance window of 25 μm aluminized kapton simultaneously serves as gas barrier and as drift electrode.

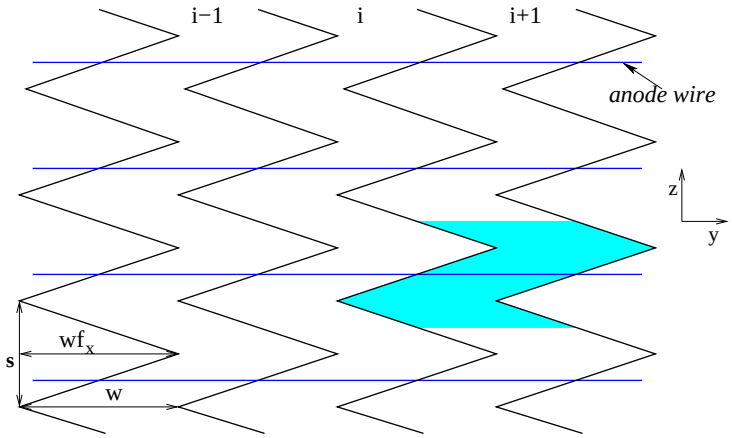

Figure 14.1: Sketch of the chevron pad plane layout.

Current- and charge-sensitive preamplifiers/shapers (PASA) were specially designed and built with discrete components. They are described in Section 5.3.3. For the results presented in the following, the charge-sensitive PASA was used. It has a gain of 2 mV/fC and a noise of about 1800 electrons r.m.s.. The FWHM of the output pulse is about 100 ns. For the readout of the DC we use an 8-bit non-linear Flash ADC (FADC) system with 100 MHz sampling frequency, 0.6 V voltage swing and adjustable baseline. The FADC sampling was rebinned in the off-line analysis in order to be closer to the final detector specifications. The data acquisition (DAQ) is the GSI-standard, MBS [2], based on the VME event builder RIO2 [3]. Usually we limited the readout of the DC to 8 pads, to minimize the data transfer on the VSB bus connecting the FADC to the event builder.

14.2 Source tests with ^{55}Fe

The prototypes have been tested with Ar- and Xe-based gas mixtures, using an ^{55}Fe X-ray source of 5.9 keV. These measurements were aimed at determining the operation point of the detector (in terms of gas gain), checking its energy resolution and for determination of the pad response function (PRF).

14.2.1 Signals and spectra

In Fig. 14.2 a collection of signals is shown, as obtained with the ^{55}Fe source for four gas mixtures: Ar,CH_4 (10%) , Xe,CH_4 (10%) , Xe,CO_2 (15%) and Xe,CO_2 (20%) . These signals are from the pad on which the collimated source was centered. The shape of the signals is a convolution of the detector signal (determined mainly by the slow ion motion) and the PASA response. The longer tails in case of Xe-based mixtures is the result of the slower ion motion. Note that the mobility of the Xe ions is almost 3 times lower than that of Ar ions [4]. From the signals illustrated in Fig. 14.2 we produce the energy spectra of the ^{55}Fe source with two methods: i) integrating the pulses over a gate of 1 μs, starting at 0.2 μs; ii) taking the maximum pulse height. In both cases we performed a sum over pads to obtain the total deposited charge, as shared by the adjacent pads.

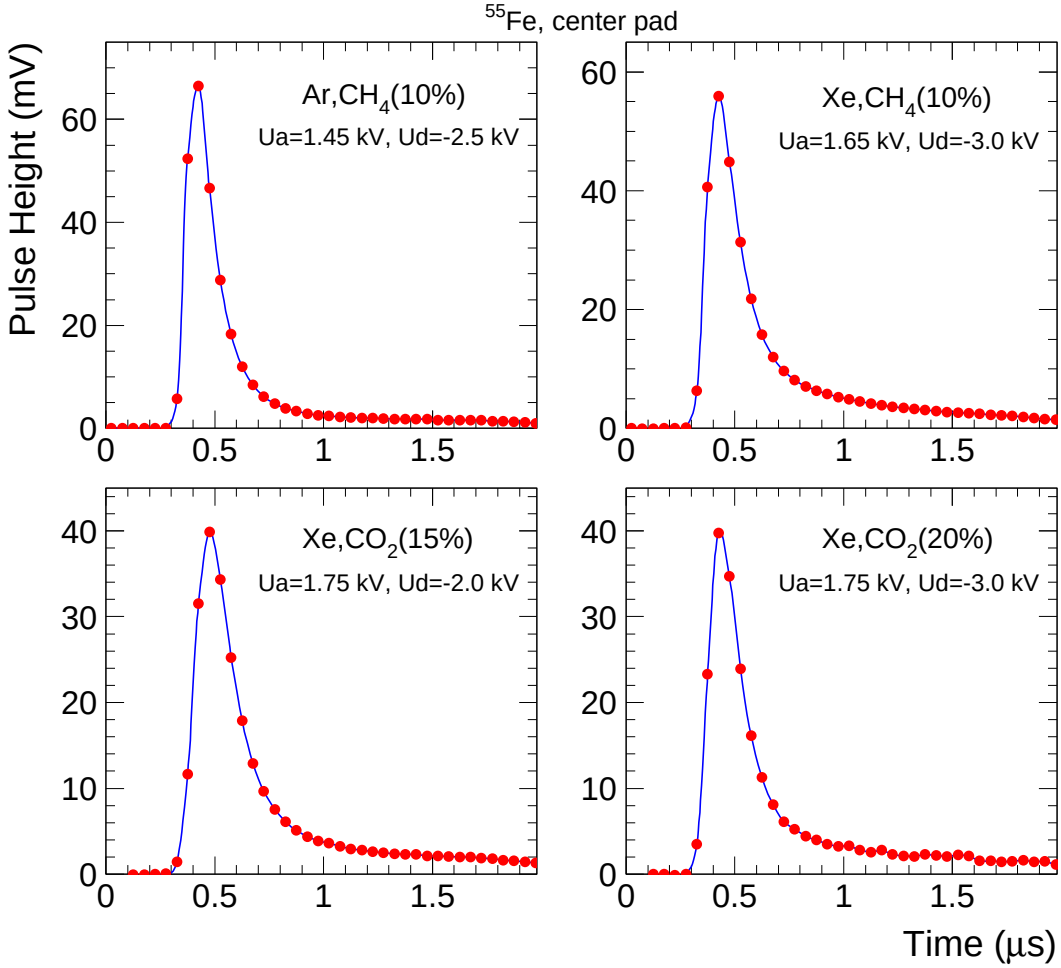

Figure 14.2: Average signals on the center pad from the ^{55}Fe source for four gas mixtures.

In Fig. 14.3 we present the spectrum of ^{55}Fe for the Ar,CH_4 (10%) gas mixture for the voltages Ua=1.45 kV and Ud=-2.5 kV, using the integrated charge Q (left panel) and the maximum pulse height PH (right panel). Besides the main peak corresponding to the full energy deposit of of 5.9 keV, the escape

peak corresponding to the partial energy deposit of 2.9 keV is clearly visible. The curves are the results of gaussian fits to the main peak. Resolutions below 10% are achieved with both methods.

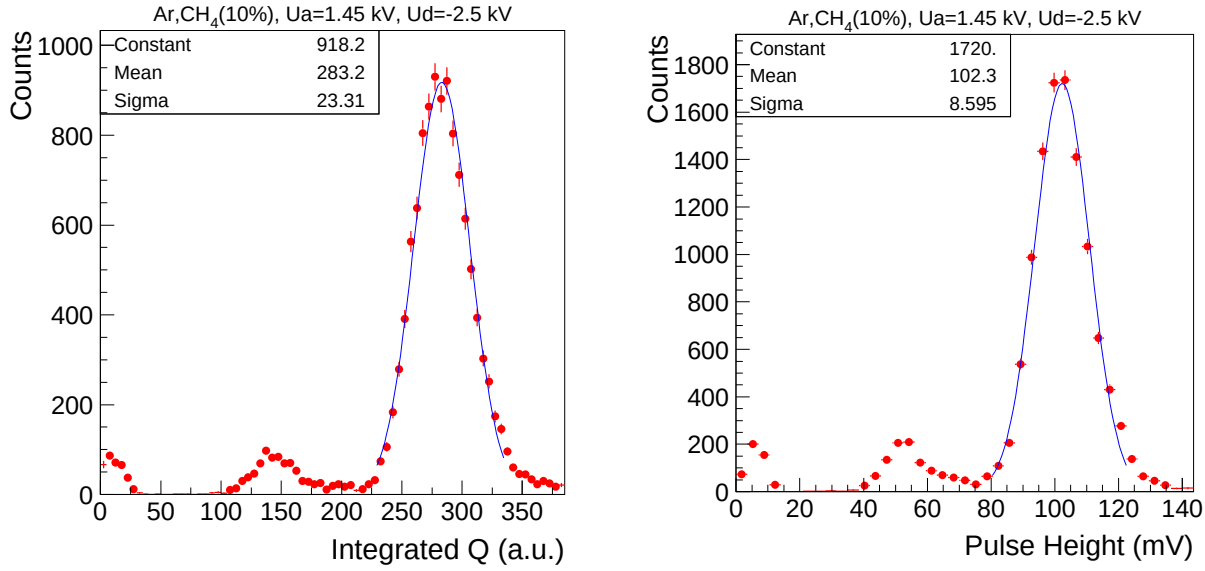

Figure 14.3: The spectra of ^{55}Fe measured with Ar,CH_4(10%). Left panel: integrated charge value, right panel: maximum pulse height. The curves are the results of gaussian fits of the main peak.

In Fig. 14.4 we present the spectra of ^{55}Fe for the case of the Xe,CH_4 (10%) mixture. In this case too, resolutions below 10% at the main peak are obtained. For roughly equal values of Q for the two mixtures (Fig. 14.3 and 14.4), the corresponding PH spectra are clearly smaller in case of Xe,CH_4 (10%) mixture. As noted above in connection to the signals presented in Fig. 14.2, this is the result of a different contribution of the tails from positive ions.

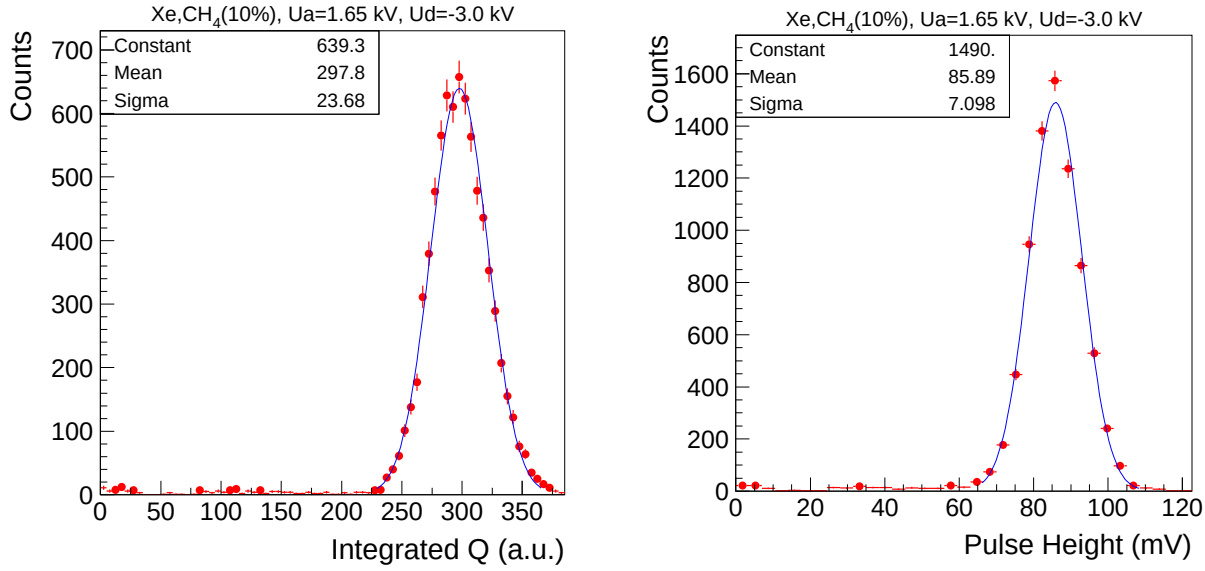

Figure 14.4: As Fig. 14.3, but for Xe,CH_4 (10%) gas mixture. Note the higher voltages (Ud=-3 kV, Ua=1.65 kV) used to achieve integrated charge values comparable to the Ar,CH_4 (10%) case (see Fig. 14.3).

In Fig. 14.5 we present the energy spectra of ^{55}Fe for the Xe,CO_2 (20%) gas mixture, for different anode voltages. Note that the resolution is in all cases below 10%. For high values of the gas gain the Xe escape peak of about 1.2 keV becomes visible.

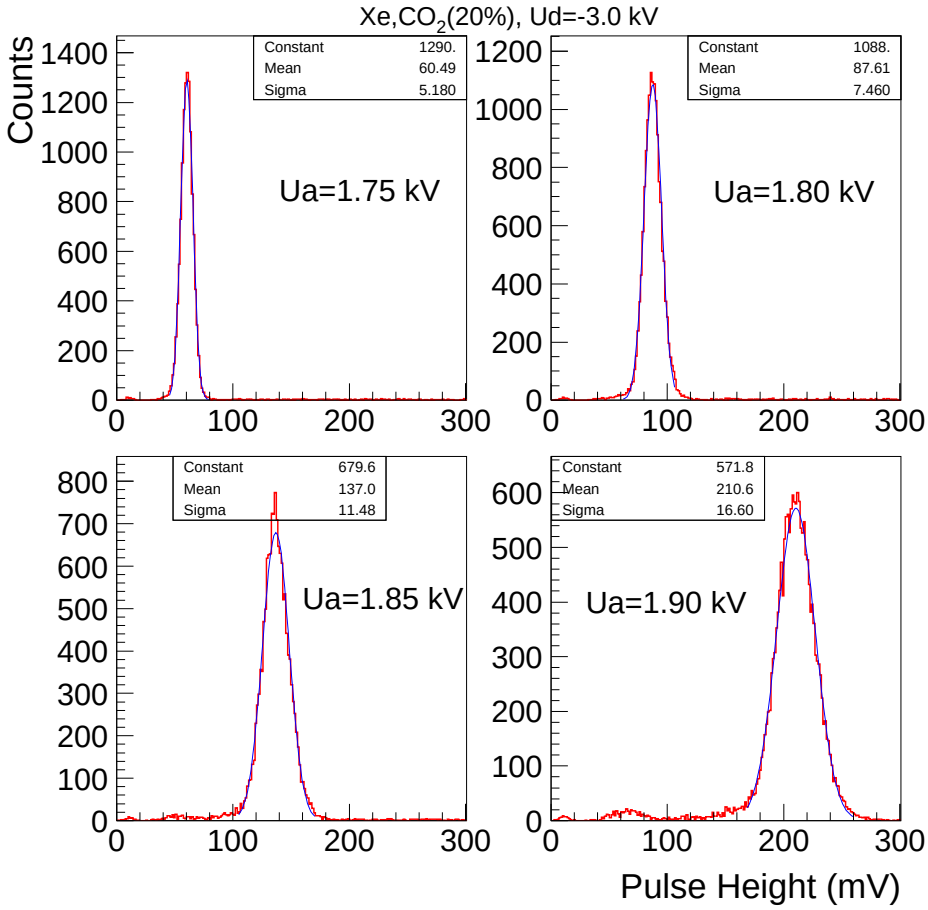

Figure 14.5: ^{55}Fe spectra measured with Xe,CO_2 (20%) for four different anode voltages.

14.2.2 Gas gain

In Fig. 14.6 we present the average energy deposit correponding to the full energy of 5.9 keV of the ^{55}Fe source as a function of the anode voltage. Four different gas mixtures (both Ar- and Xe-based) are compared, both in terms of the average pulse height and of the average integrated charge.

The gas gain for each anode voltage was determined in a separate measurement by measuring the anode current and the activity, using a non-collimated ^{55}Fe source (to get high activity for good precision of the current measurement). A pulse height of 100 mV corresponds to a gas gain of about 10^4 in case of the Ar mixture. For the Xe mixtures, due to a larger primary number of electrons ($\approx$270, compared to $\approx$220), the gas gain is correspondingly lower at the same pulse height. The drift voltages were not kept constant and this influences the gas gain (see Section 14.4). Despite this effect, one can see that different anode voltages are needed in order to achieve the same gain, depending on the gas mixture. In case of CO_2 quencher, the higher voltage necessary for Xe,CO_2 (20%) compared to Xe,CO_2 (15%) is almost compensated by the larger drift voltage, which contributes to the gain (see below, section 14.4).

14.2.3 Pad response function

The PRF is a measure of the degree of sharing of the image charge on the cathode plane by adjacent pads. The PRF, measured using the ^{55}Fe source, is presented in Fig. 14.7. Shown is the ratio of the charge (integrated over a gate of 1 μs) on the central pad (Q_{cen}) to the sum of charges on the center pad and two neighbouring ones on each side (Q_{tot}) as function of the position of the hit. This position, y, is expressed relative to the pad width, w, which is 10 mm in our case. It has been calculated using a formula derived

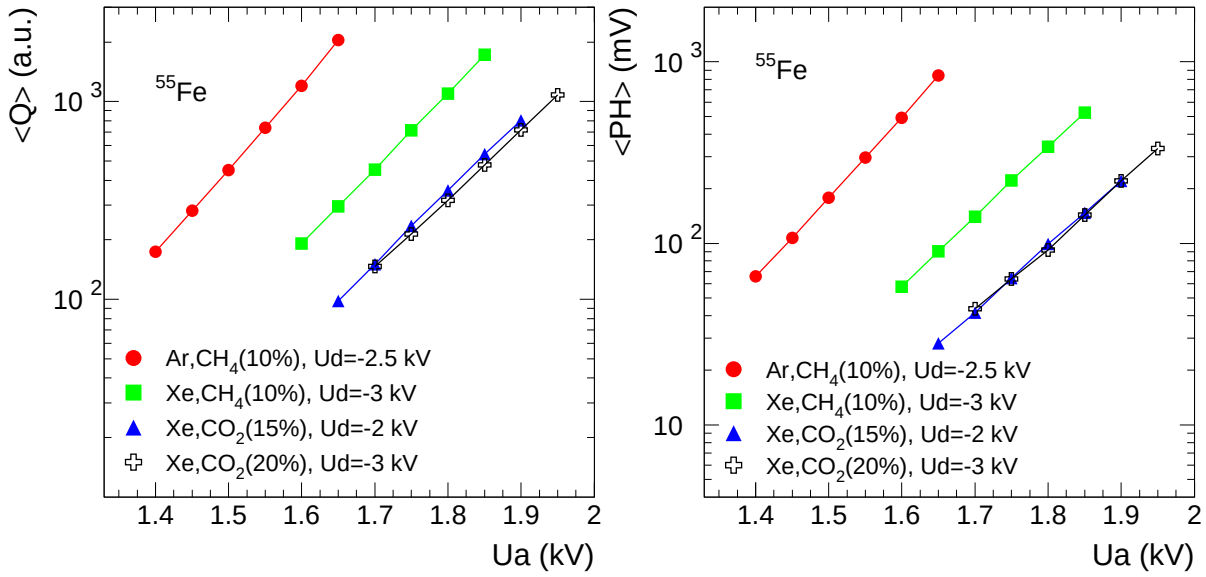

Figure 14.6: Gain curves for four gas mixtures. Average integrated charge (left panel) and average pulse height (right panel) of the main peak of ^{55}Fe as function of the anode voltage. An average pulse height of 100 mV corresponds to a gas gain of $\approx 10^4$ in case of Ar,CH_4 (10%) .

assuming a gaussian PRF [5, 6]:

$$y = \frac{w}{2} \frac{\ln(Q_{i+1}/Q_{i-1})}{\ln(Q_i^2/Q_{i+1}Q_{i-1})}, \tag{14.1}$$

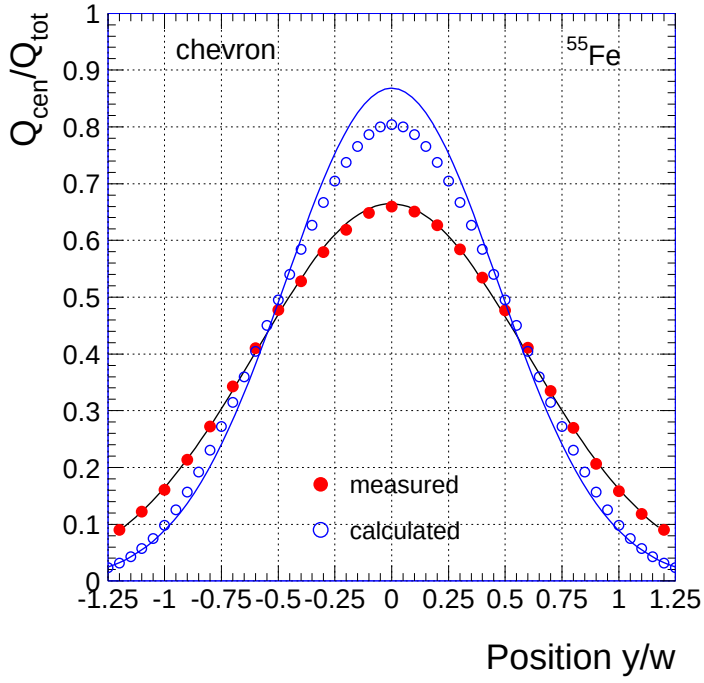

Figure 14.7: Pad response function: measured with ^{55}Fe source, for Ar,CH_4 (10%) (dots) and calculated (circles). The continuous lines are results of gaussian fits.

where Q_i is the integrated signal for pad i (which is the pad with the largest signal). The full dots denote the measured values, while the circles are for calculated values using the Mathieson recipe [7]. It is evident that the measured PRF does not agree with the calculated one, which is clearly narrower. This broadening is the effect of capacitive cross-talk between adjacent PASA channels which is discussed below. The continuous lines are results of gaussian fits. While the measured PRF is perfectly approximated by a gaussian (with $\sigma=0.6\times w$), the calculated one is not. The gaussian shape of the measured PRF could be an artifact of the method, but a different method, namely moving the collimated source across the pad and recording the above ratio as a function of position, gives identical results. Note that in the derivation of the Mathieson formula a symmetric amplification gap is assumed. The transparency of the cathode grid may destroy this assumption. From our most recent studies using different cathode wire pitches (see Section 14.4) we can rule out that the density of the cathode grid has a major influence on the measured PRF.

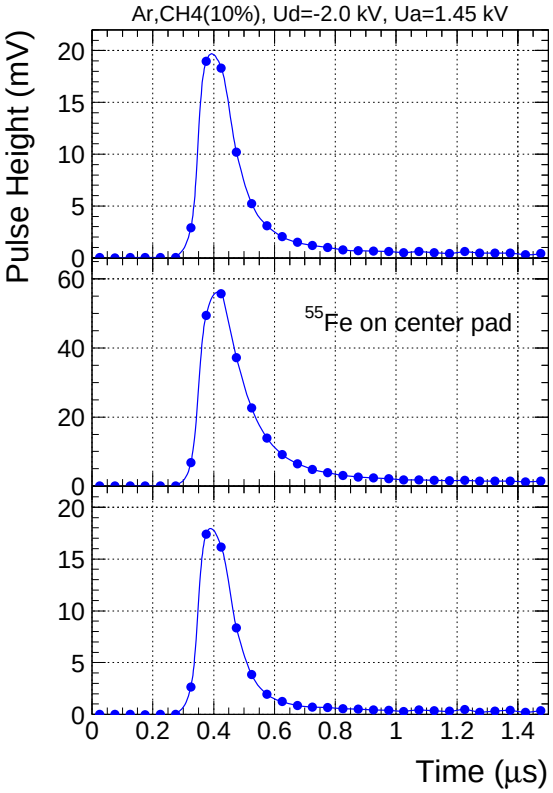

Figure 14.8: Signals produced by the ^{55}Fe source on three adjacent pads.

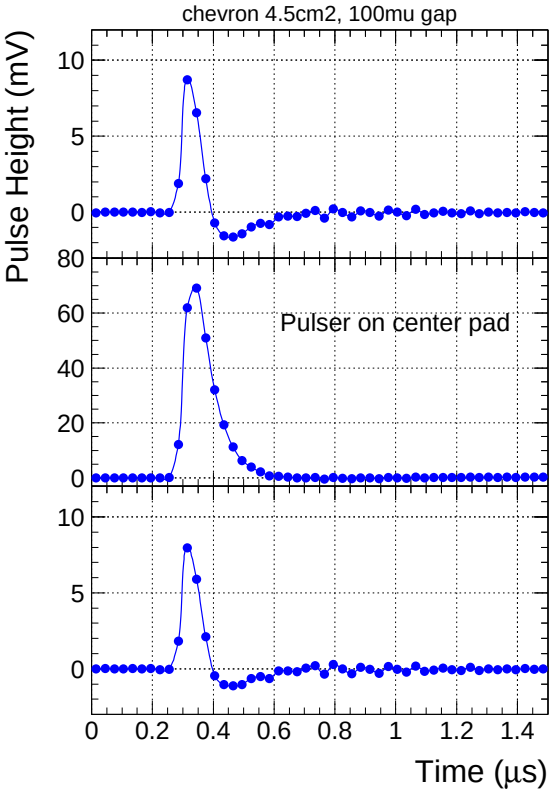

Figure 14.9: Signals on three adjacent pads from a pulser signal on the center pad.

To understand the reason of the discrepancy between the measured and calculated PRF, we looked in detail into the effect of the preamplifier cross-talk. We have noticed early on that the tail of ^{55}Fe pulses in the neighbouring pads has a time decay smaller compared to the center pad. Fig. 14.8 shows an example of the average pulses (the average is done over many events) on three pads, when a collimated ^{55}Fe source was centered on the middle pad. The different time behaviour is the result of the cross-talk between two neighbouring channels of the PASA, due to the pad to pad capacitance. This is demonstrated in Fig. 14.9, where we present average signals on three pads when a step signal (28 mV on 1 pF, 5 ns rise time) from a pulse generator was fed to the center pad, directly on the detector. In this case the neighbouring channels should ideally see no signal, since there is no charge sharing. Instead, a bipolar cross-talk is seen. On this spurious signal the true ^{55}Fe signal from pad sharing would add, creating

the shapes presented in Fig. 14.8. One observes about 12% cross-talk in the pulse height in each of the adjacent channels. This cross-talk figure would explain the difference of the measured PRF compared to the calculated one. However, when integrating over 1 μs (as it was done for the ^{55}Fe signals when deriving the PRF), the cross-talk is reduced to 4%. Note that without load the channel to channel cross-talk is below 0.5%. In a second step we investigated the cross-talk as function of rise time of the input pulse (apart of 5 ns, we used 20 and 50 ns) and of the shaping time of the PASA and found only little dependence. The cross-talk is mainly determined by the input impedance of the PASA, which was in the present case about 1 kΩ. Naturally, the cross-talk increases as a function of the capacitive coupling between neighbouring channels. We established that a channel to channel capacitance of 8 pF is reproducing the cross-talk measured on the detector (Fig. 14.9), in agreement with our measurements and calculations of the pad to pad capacitance.

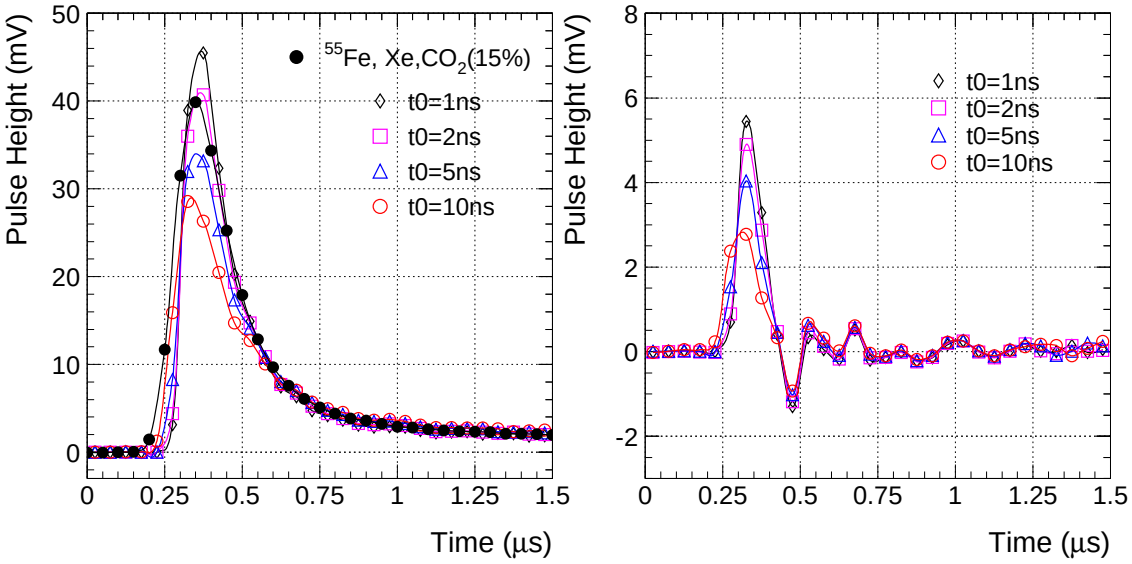

Figure 14.10: Pulser signals on the main pad and on a neighbouring one for different shapes of the input pulse. Note the different scales for the *y* axis.

The signal from the detector may be quite different from a simple step pulse. To check this particular detail, we injected pulses that simulate the time evolution of the signals from the real detector. These pulses have a fast rise time, followed by a slow logarithmic rise. The measured signals for the main pad (left panel) and neighbouring pad (right panel, note the different scale on the *y* axis) are presented in Fig. 14.10. The different open symbols correspond to different time constants of the fast component, while the dots are for a measured ^{55}Fe signal. The values of the pulse height cross-talk are very similar to those seen with the simple step pulse (Fig. 14.9). However, one can notice that the shape of the cross-talk signal is quite different in the present case. Although the time dependence of the signal on the neighbouring pad (right panel in Fig. 14.10) is different compared to the one of the main pad (left panel), no undershoot is seen for this more realistic input pulse. When integrating over 1 μs, the cross-talk is about 4%, identical to the case of the step input pulse. In order to improve our understanding of the discrepancies between the observed and the calculated PRF, the problem of the cross-talk is being investigated further. However, the present results are obtained with a preamplifier/shaper which is different than the final one (see Chapter 5). This integrated version is particularly optimized for a low input impedance and measurements on the detector will follow soon.

14.3 Beam tests

The measurements have been carried out at beam momenta between 0.7 and 2 GeV/c [8]. The electron content of the beam varies as function of momentum and is of the order of 2-3% for 1 GeV/c. We used mixed electron-pion beams provided by the secondary pion beam facility at GSI Darmstadt [9].

14.3.1 Setup

The setup used for the beam tests is sketched in Fig. 14.11 (see also Color Fig. 8). It comprises the following detectors:

- a one-layer TRD, composed of a radiator (R) and a readout chamber (drift chamber, DC).
- three scintillator counters (S0, S1, S2), used for beam definition. Their dimensions are 5×10 cm^2.
- a gas-filled threshold Cherenkov detector (Ch), 2 meters in length, read out via a mirror by two photomultipliers, for electron identification.
- a Pb-glass calorimeter (Pb), with dimensions 6×10 cm^2 and a depth of 25 cm (equivalent to 10 X_0) for electron validation.
- a multiwire proportional chamber (MWPC) [10] with a 20×20 cm^2 active area, used for monitoring the beam profile.
- two silicon strip detectors (Si1, Si2) with active area of 32×32 mm^2. Each has strips of 50 μm pitch in both x and y direction, representing a total of 1280 channels per detector. As these signals are read out in a zero-suppression mode, they do not contribute significantly to the data volume. They are used off-line for tracking for the position reconstruction using the DC (see Section 14.3.7).

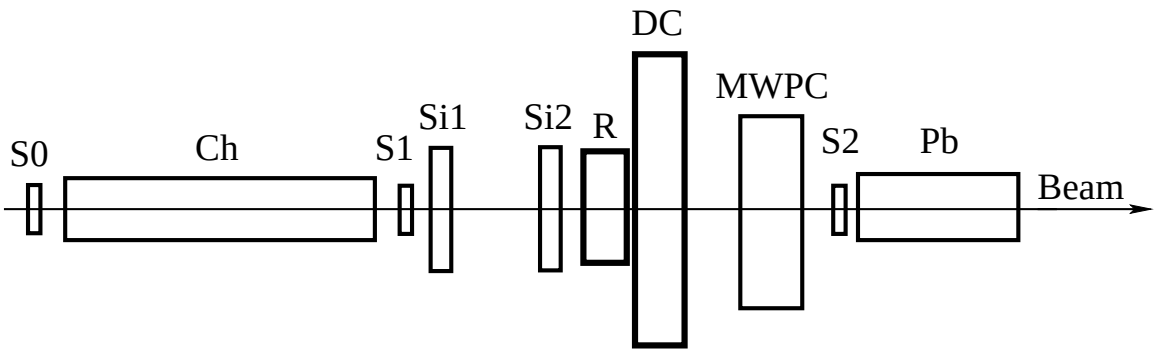

Figure 14.11: Sketch of the setup used for the beam tests (not to scale). The different components are explained in the text.

The beam trigger was defined by the scintillator counters S1 and S2, to which the Cherenkov signal was added as the electron trigger. Both electron and pion events are acquired simultaneously by using appropriate pion scaledown factors. Off-line the events were selected using the correlation between the signals delivered by the Cherenkov and the Pb-glass detectors, shown in Fig. 14.12 for the momentum of 1 GeV/c. As seen, by requiring threshold signals in both detectors (the lines in Fig. 14.12) one can isolate clean samples of pions and electrons. For this momentum we used a pion scaledown factor of 8. Measured with the MWPC, the horizontal size of the beam was about 4.5 cm FWHM.

The gases used for the DC were Xe-based mixtures. We used both CH_4 (10%) and CO_2 (15% and 20%) quenchers. We selected the anode voltages such that the gas gain of the chamber was in the range of 5000 to 8000 for most of the measurements, except when we intentionally varied it for some particular

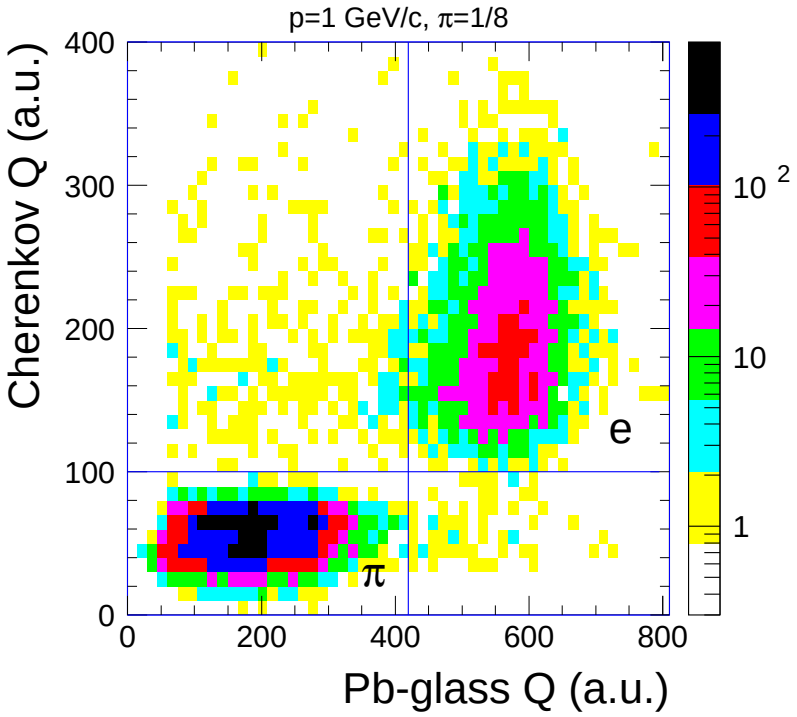

Figure 14.12: The correlation of the signals from the Cherenkov detector and the Pb-glass calorimeter. The thresholds used to identify negative pions and electrons are indicated.

studies (see below). The oxygen content in the gas was continuously monitored and kept below 10 ppm using a flow of 2-3 liters/hour.

14.3.2 General properties of the detector

Distributions of average pulse height, $\langle PH \rangle$, as a function of drift time for different drift voltages are shown in Fig. 14.13 for pions of 1 GeV/c momentum. Three Xe-based gas mixtures are compared: 15% CO_2, anode voltage Ua=1.75 kV (upper left panel), 20% CO_2, Ua=1.80 kV (upper right panel) and 10% CH_4, Ua=1.75 kV (lower panel). Note that in the case of Xe,CO_2 (20%) the incidence was perpendicular to the anode wires, while in the other two cases it was at about 17° with respect to the normal to the anode wires.

The time zero has been arbitrarily shifted by about 0.4 μs to have a measurement of the baseline. Note that the average pulse height in the drift region exhibits a slight increase as a function of drift time. This is the result of build-up of detector currents from ion tails, convoluted in addition with the response of the preamplifier. The peak at the beginning of these distributions originates from the primary clusters in the amplification region, where the ionization from both sides of the anode wires contributes to the same time channel. These characteristics have been reproduced by simulations of detector signals using GARFIELD [12]. The drift voltages have been tuned to cover a similar range of drift velocities around 1.5 cm/μs. The voltages are different for the mixtures investigated (especially between the two quencher gases, CO_2 and CH_4), as expected. Notice also that the behaviour with the field strength is different (see below).

Analysis of the distributions presented in Fig. 14.13 allows a rough estimate of the drift velocities for the different mixtures. This accuracy is limited by the accuracy in assigning the beginning of the drift region out of the tail of the signals in the amplification region. The results (open symbols) are plotted in Fig. 14.14 as function of the drift field for three Xe-based gas mixtures, along with calculations using GARFIELD/MAGBOLTZ [12, 13] (full symbols). While for the CO_2 mixtures our drift fields of the

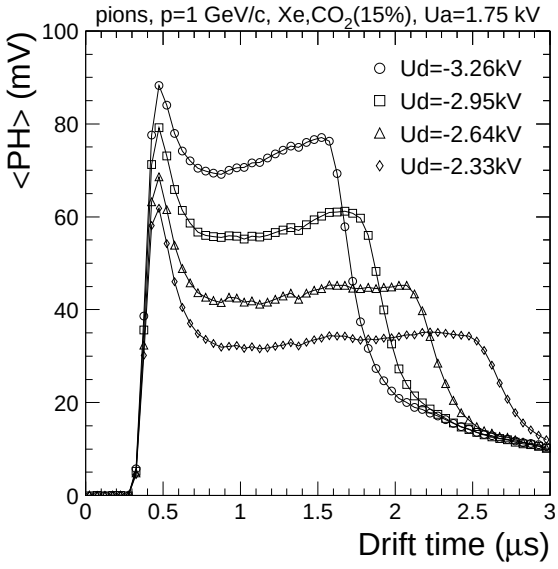

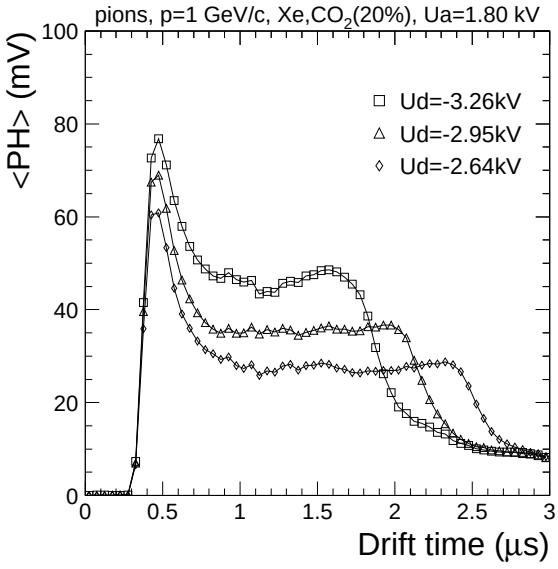

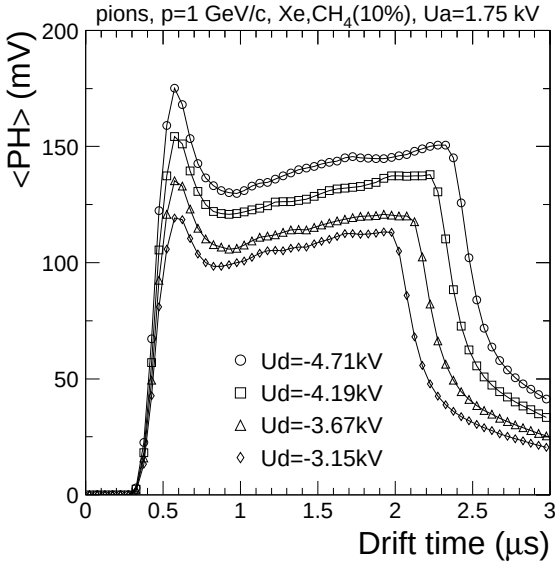

Figure 14.13: The average pulse height as function of drift time for different drift voltages. Three Xe-based gas mixtures are compared: CO_2 (15%), for the anode voltage Ua=1.75 kV (upper left panel), CO_2 (20%), Ua=1.80 kV (upper right panel) and CH_4 (10%), Ua=1.75 kV (lower panel).

order of 1 kV/cm correspond to the rising part of the distribution, in case of the CH_4 quencher we are already in the slowly decreasing region after the first maximum. Within the limitations of the method, one can say that the calculations reproduce the drift velocities in case of CO_2 mixtures, but there seems to be a disagreement for the CH_4 case. For this particular case, we include in the comparison the measured data of Christophorou et al. [14], to which our values are compatible. Note that a more recent set of measurements [15] are significantly different. We mention that the water content, which influences the drift velocity quite strongly, was about 150 ppm in case of CO_2 mixtures, but was not measured in case of Xe,CH_4 (10%) .

One can notice in the distributions presented in Fig. 14.13 that the relative magnitude of the peak to the plateau is varying as a function of the drift field. This is due to the compression of the same signal in progressively shorter time intervals. In detail, this behaviour seems to be mixture dependent. A detailed look at these facts is presented in Fig. 14.15. Here we show the drift field dependences of the measured

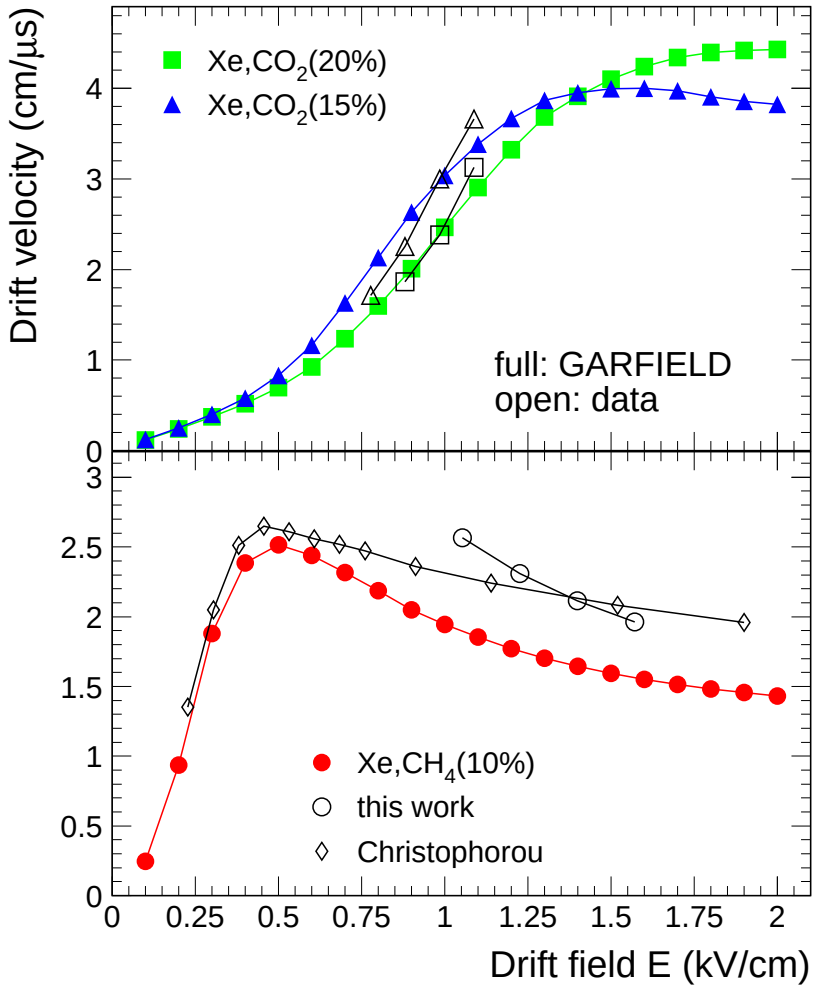

Figure 14.14: The dependence of the drift velocity on the drift field for three Xe-based gas mixtures. The data extracted from Fig. 14.13 (open symbols) are compared to calculations using GARFIELD/MAGBOLTZ [12, 13] (full symbols). For the Xe,CH_4 (10%) case we include in the comparison the measured data of Christophorou et al. [14].

charges in the drift region, Qd and in the amplification region, Qa. These quantities are integrals of the pulse height over the timespan of the plateau and peak, respectively. The sum of them (upper panel, note the logarithmic scale) is increasing as a function of drift field, a result of increasing gas gain (see Section 14.4). The ratio Qd/Qa is presented in the lower panel. Its dependence on the drift field, different for CO_2 and CH_4 quencher, is the effect of the different drift velocity variation, as seen in Fig. 14.14. The decreasing of this ratio for higher drift velocities may already point to a space charge effect (see below), which is more pronounced in case of an electron arrival more compressed in time.

Figure 14.16 shows the dependence of Qd+Qa and Qd/Qa as a function of the anode voltage. The integrated charge (upper panel, notice the logarithmic scale) is exhibiting the gas gain dependence on the anode voltage (see Section 14.2.2). The ratio Qd/Qa, shown in the lower panel, gives an indication of the gas gain saturation (lower gain for the late electrons due to the screening of the anode potential by the ions from previous clusters) as function of gas gain. For no gain saturation this ratio is flat. The small decrease points to a small gain saturation. However, this conclusion is somewhat ambigous because of the uncertainty in delineating the amplification region, which may extend into the drift region as function of increasing anode voltage. We note though, that the distributions of the average pulse heights from

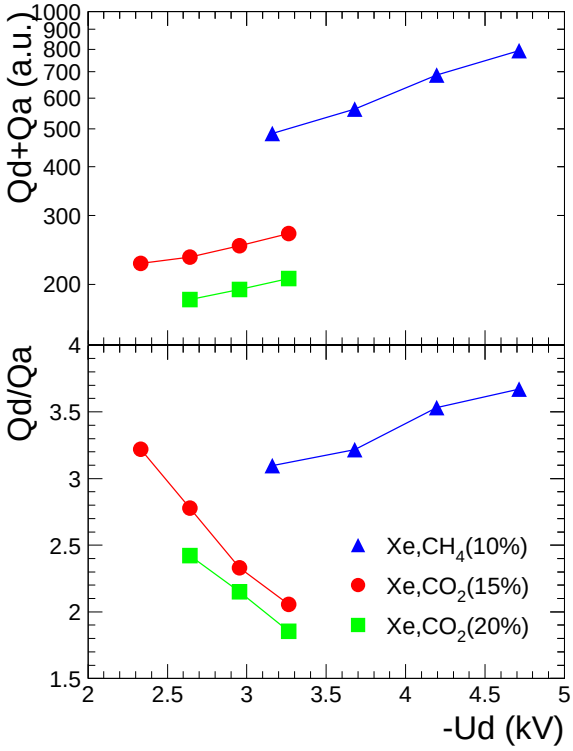

Figure 14.15: Summary of drift field dependences of the charges measured in the drift (Qd) and amplification (Qa) region.

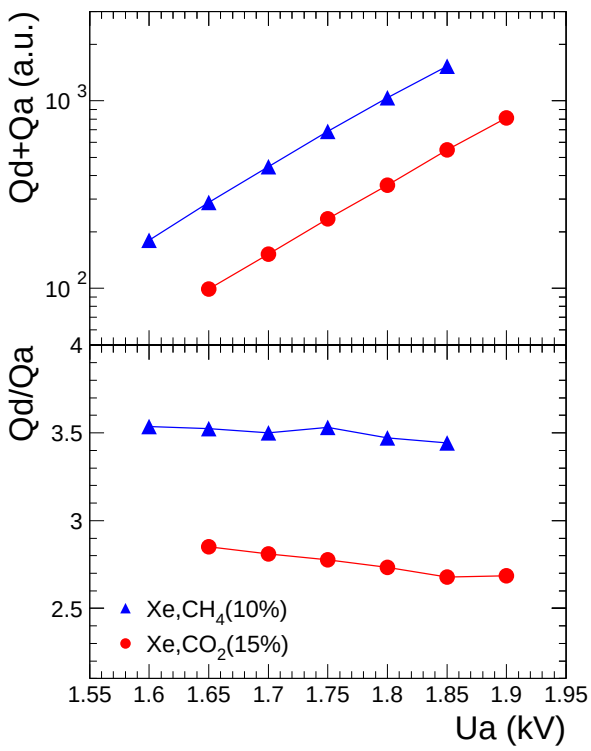

Figure 14.16: Summary of anode field dependences of the charges measured in the drift (Qd) and amplification (Qa) region.

which the ratio Qd/Qa was derived are very similar for all the anode voltages under consideration, thus pointing to a genuine gain saturation effect. The effect is rather small because the incident angle in this case was 17° with respect to the normal to the anode wires.

In Fig. 14.17 we present an example of the evolution of the average pulse heights as a function of drift time with respect to the incident angle along the anode wires. These distributions were recorded for a moderate gas gain of about 6000. However, decreasing the angle towards normal incidence, the signal gets progressively attenuated as function of drift time. This is a clear signature of the gas gain saturation, which is a local effect. When spreading the primary electrons along the anode wire, the effect becomes less and less important. Simulations confirm this interpretation (see Chapter 4). Note that the signal in the amplification region (the peak) is independent of the angle (there is no relative normalization of the data for different angles), since there are no precursor avalanches that can screen it.

In Fig. 14.18 we present the summary of the above effects. The ratio Qd/Qa is plotted as a function of the incident angle along the anode wires for three values of gas gain, separated by factors of 2.35. The variation of the ratio with the angle is very pronounced for small angles, while a saturation is reached at larger angles due to the locality of the screening, as mentioned above. The ratio has a stronger variation for larger gains, as expected. As we will show in Section 14.3.6 the gas gain saturation is affecting the pion rejection performance of the detector. Due to these effects, we envisage to operate the chambers at the lowest possible gas gain (around 5000).

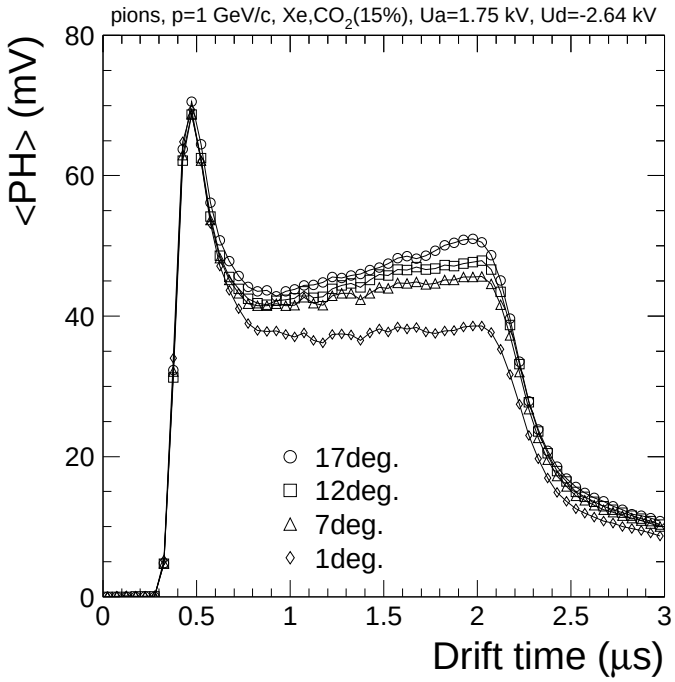

Figure 14.17: Average pulse heights as function of drift time for different incident angles along the anode wires.

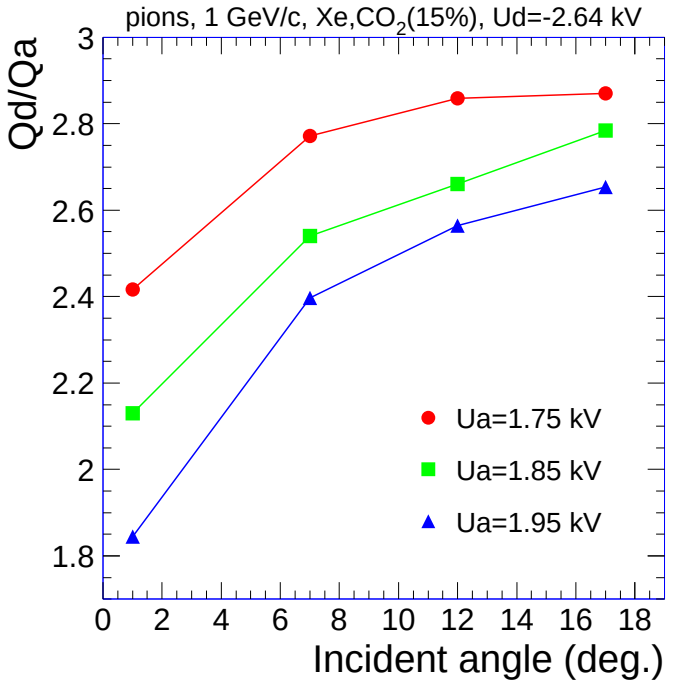

Figure 14.18: Ratios of charges recorded in the drift and amplification regions as function of incident angle along the anode wires for three values of the gas gain.

14.3.3 Pion and electron distributions

In this section we present typical distributions for pions and electrons for a momentum of 1.0 GeV/c and a fibre radiator. Unless specified, the incident angle is 17° with respect to the normal to the anode wires.

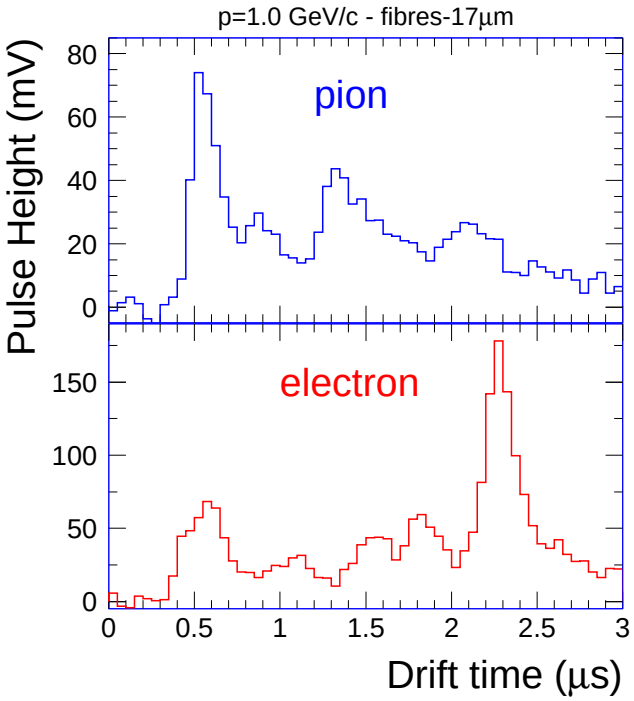

Figure 14.19: Typical signals as a function of drift time for a pion and an electron for the momentum of 1.0 GeV/c. Note the different scales on the vertical axes.

In Fig. 14.19 we show an example of the signal distribution as a function of drift time for a pion and an electron. Here and in what follows we are using a time bin of 50 ns, a value smaller than that of the final configuration of the TRD in ALICE. We checked that by increasing the time bin from 50 ns to 100 ns the performance of the detector with respect to the pion rejection does not change. Note the different magnitude of the two signals and, for the electron, the big cluster at late drift time, possibly corresponding to a TR photon absorbed early near the entrance of the DC. Detailed simulations [11] showed that the electron identification is significantly improved by using, along with the pulse height, the drift time information (see below).

We show in Fig. 14.20 the drift time distribution of the average pulse height summed over the adjacent pads, $\langle PH \rangle$, for pions and electrons in case of a fibre radiator with 17 μm fibre diameter (thickness X=0.3 g/cm^2). For electrons (square symbols) there is a significant increase in the average pulse height at later drift times, due to preferential absorption of TR near the entrance of the DC. The dashed line in Fig. 14.20 is the expected pulse height distribution for electrons without TR; it has been obtained by scaling the pion distribution with a factor of 1.45, measured in a separate experiment without radiator. Pulse height distributions as a function of drift time have been reported by other experiments [16, 17, 19, 20]. A decrease of the pulse height as a function of drift time was observed in all those cases and it was attributed to electron attachment [20]. We stress that it is for the first time that the expected signal is directly seen in such a detector.

The distributions of the integrated energy deposit are shown in Fig. 14.21 for pions and electrons for a momentum of 1 GeV/c, in case of a 17 μm fibres radiator. The pure Landau distribution exhibited by pions is spread towards higher values in the case of electrons due to the contribution of the TR.

The distributions of the position of the largest cluster found in the drift region are shown in Fig. 14.22. The detector depth is expressed here in time bin (50 ns) number, where the counting starts at 0.75 μs (see Fig. 14.20) and increases towards the entrance window for a total of 32 time bins. The trends seen in Fig. 14.20 are present in these distributions as well. For the case of electrons the probability to find the largest cluster is strongly increasing towards the entrance of the detector (higher time bin number) due

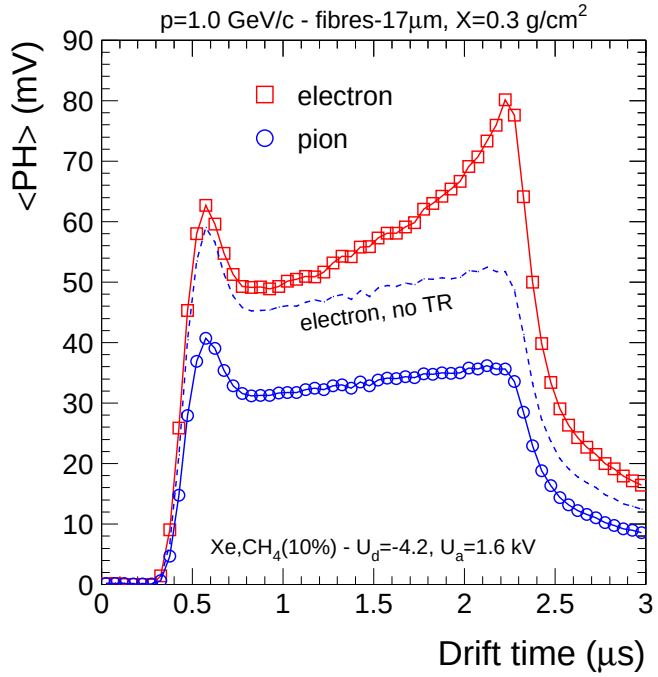

Figure 14.20: Average pulse height as a function of the drift time for pions and electrons for a radiator of 17 μm diameter fibres at the momentum of 1 GeV/c. The dashed line represents the energy deposit by pure ionization in case of electrons (see text).

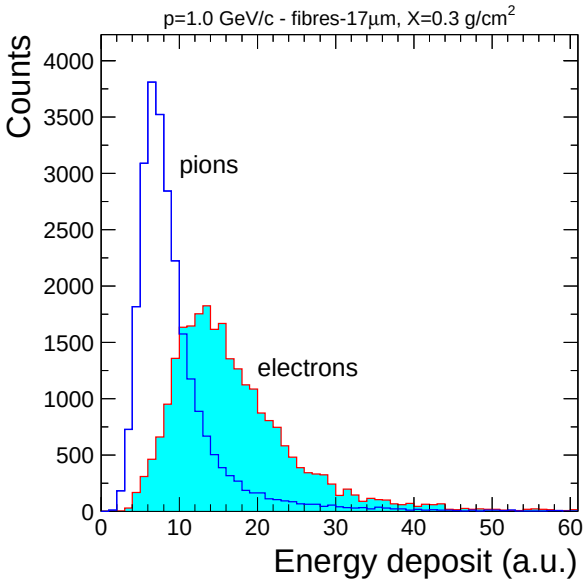

Figure 14.21: Integrated energy deposit for pions and electrons for a momentum of 1.0 GeV/c. A radiator with 17 μm fibre has been used.

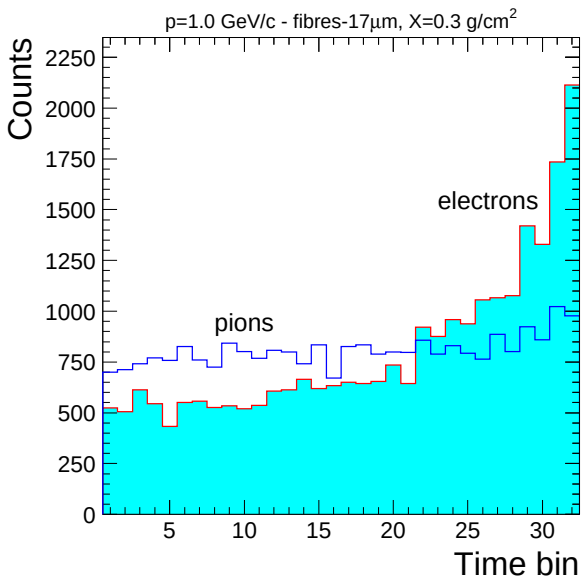

Figure 14.22: The distributions of position of the largest cluster found in the drift region for pions and electrons.

mainly to the contribution of TR, while for pions there is only a slight increase which is due to the ion and preamplifier tail build-up explained above. The distributions presented in Fig. 14.21 and Fig. 14.22 are normalized to the same number of events.

14.3.4 Radiator comparison

Various radiators were tested: regular foils of polypropylene (PP), mats of irregular PP fibres with various fibre diameters (between 15 and 33 μm) and foams of different material type: PP, polyethylene (PE) and Rohacell (RC). These radiators spanned a large range in densities and structural properties, as one can see in Table 14.1. The quantity d quoted here is the linear dimension of the structural unit, which for the foils means foil/gap thicknesses, for the fibres the diameter and for the foams the typical pore size. The variation in total thicknesses is also large, from 3 to 10 cm.

Table 14.1: The properties of various radiators.

Name	Material	ρ (g/cm^3)	d (μm)
foils120	PP	120 foils	20/500
foils220	PP	220 foils	25/250
fibres17	PP	0.074	17
fibres20	PP	0.05	15-20
RG30	PP	0.03	1300
RG60	PP	0.06	700
WF110	RC	0.11	700
HF110	RC	0.11	≈75
HF71	RC	0.07	≈75
IG51	RC	0.05	≈75
HF31	RC	0.03	≈75
EF700	PE	0.12	800
S-HF110	RC/PP	0.086	sandwich
S-HF71	RC/PP	0.073	sandwich

To study the relative performance of the various radiators presented in Table 14.1 we have classified them according to the equivalent thickness into two classes, with roughly X=0.3 g/cm^2 and X=0.6 g/cm^2 (the radiation length for some this materials is provided in Chapter 3). The measurements are summarized in Fig. 14.23 in terms of the ratio between the average pulse height of electrons and pions, $\langle PH \rangle_e / \langle PH \rangle_\pi$, as function of detector depth. The detector depth is divided here into 5 zones, where zone 0 is the amplification region and each of the others is a quarter of the chamber's drift region (drift time between 0.75 and 2.35 μs in Fig. 14.20). The numbering goes from the cathode wire plane towards the entrance of the DC. In this representation, a better relative performance of the radiator amounts to a higher ratio between electron and pion pulse height, while the increase towards the entrance of the detector gives information about the characteristics of the spectrum of the TR. The case of no TR would produce a flat distribution at about 1.45 for the momentum of 1 GeV/c. These measurements were performed using the Xe,CH_4 (10%) gas mixture.

The most important conclusion from Fig. 14.23 is that the fibre radiators exhibit performances comparable to that of radiators with foils, being only slightly worse. Taking into account that the foil radiators are significantly lighter than the other radiators in both cases (with X=0.22 g/cm^2 and X=0.5 g/cm^2, respectively), our conclusion is in agreement with previous studies [17]. The fibres with lower density, fibres20, produce slightly more TR compared to the more dense ones, fibres17. In a separate study we have found that the fibre diameter influences the TR yield only marginally. Radiators composed of fibres with 17 and 33 μm diameter show similar TR performance for the same density and thickness. We note that in a previous measurement it was found that the momentum dependence of the pion rejection is influenced by the fibre diameter [23].

The performance of the foams is comparable to the fibres only in the case of the light PP foam, RG30.

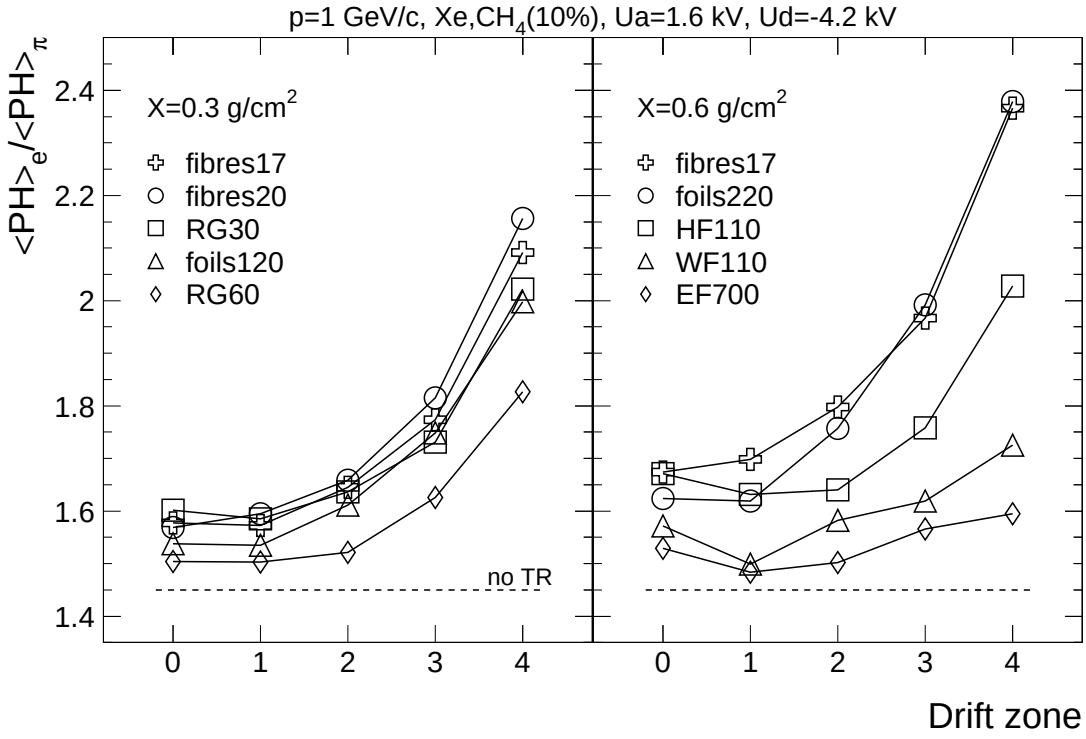

Figure 14.23: Average relative electron/pion pulse height as function of the drift zone for various radiators (see Table 14.1) of two thicknesses for the momentum of 1 GeV/c. These measurements were performed using the Xe,CH_4 (10%) gas mixture. See text for details.

However, in this case the 10 cm thick radiator is a serious disadvantage (at least for the ALICE TRD). The more packed version of the same material, RG60, produces significantly less TR (furthermore, it is thicker, X=0.36 g/cm^2). We found that the Rohacell foams HF110 and WF110 exhibit very different features. Contrary to the expectations, it is the version with less structure (invisible pores), HF110, that gives higher TR yield. The other Rohacell foam, WF110, as well as the Ethafoam, EF700, are basically excluded as radiator candidates. Judging by their apparent structure, these foams would have been expected to deliver reasonably good TR performance. Their low TR yield may be the consequence of a higher absorption due to their chemical compositions. In particular, especially concerning their TR spectra, Ethafoams were established early on as promising candidates for radiators [18]. Note that it was found that even PE foil radiators exhibit poor TR performance [17], presumably due to a low TR yield. In general, similar results concerning the relative comparison of different radiator materials have been obtained in other experiments [17, 21, 22].

After the first step of selecting the best candidates for a radiator, we have extended our study towards finding a more realistic radiator that would satisfy both the TR performance and the mechanical stability requirements (see Chapter 3). We have investigated sandwich radiators composed of 17 μm fibres and Rohacell foams. The results are presented in Fig. 14.24, where we compare the ratio of electron to pion pulse heights as function of drift zone for sandwich radiators (S-X) and for pure Rohacell foams and pure 17 μm fibre radiators. A measurement without radiator is included. This comparison is done for a fixed geometrical thickness of 4.8 cm. The pure fibre radiator has a thickness of only 4 cm, to allow direct comparison to our previous measurements. The sandwiches contain 3.2 cm of fibres between 2 sheets of Rohacell foams of 0.8 cm each. The detection gas was Xe,CO_2 (15%) . It is evident that all cases

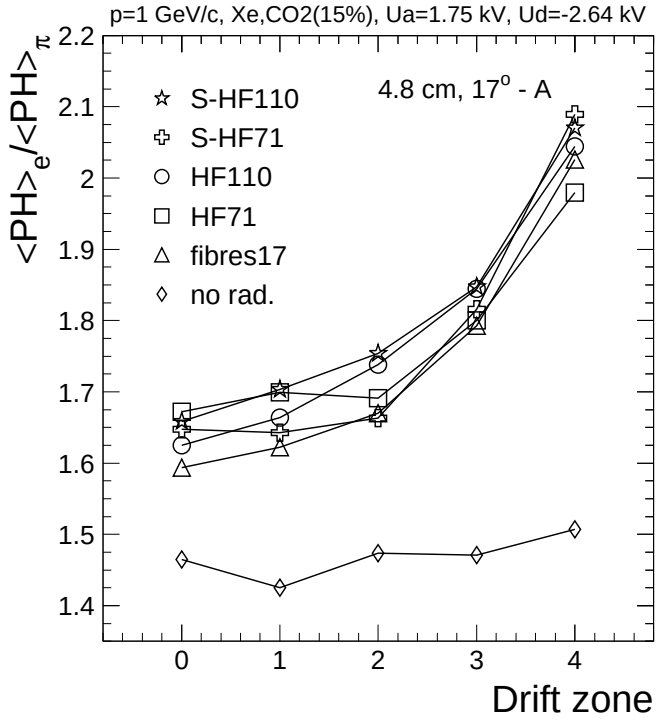

Figure 14.24: Average relative electron/pion pulse height as a function of the drift zone. Pure Rohacell foams and 17 μm fibres radiators are compared to sandwich radiators (S-X) built from both materials. The detection gas was in this case Xe,CO_2 (15%) mixture. A measurement without radiator is included.

under study yield very similar TR performance, essentially because of their different densities within the constraint of the same thicknesses (with the exception of pure fibres radiator, as mentioned).

14.3.5 Pion rejection performance

The distributions presented in Fig. 14.21 and Fig. 14.22 have been used as probability distributions in simulations aimed at determining the pion rejection factor for the proposed configuration of the ALICE TRD. To extract the pion rejection factor we have studied three different methods: i) truncated mean of integrated energy deposit, TMQ; ii) likelihood on integrated energy deposit (see Fig. 14.21), L-Q [23]; iii) two-dimensional likelihood on energy deposit and position of the largest cluster found in the drift region of the DC (see Fig. 14.22), L-QX [19].

For a certain energy deposit E_i in layer i, $P(E_i|e)$ is the probability that it was produced by an electron and $P(E_i|\pi)$ is the probability that it was produced by a pion. The likelihood (to be an electron), L, is given by:

$$L = \frac{P_e}{P_e + P_\pi} \quad , \tag{14.2}$$

where

$$P_e = \prod_{i=1}^{N} P(E_i|e) \quad ; \quad P_\pi = \prod_{i=1}^{N} P(E_i|\pi). \tag{14.3}$$

We assume that the six layers have identical performance as represented by the measured distributions of Fig. 14.21 and Fig. 14.22 and that there is no correlation between the layers. Both the truncated mean (the truncation is done by excluding the highest value of the integral energy deposit among the layers) and the likelihood distributions (Eq. 14.2) were constructed over the six layers for the same number of simulated pion and electron events. Cuts on electron efficiency were imposed on these distributions and

the pion efficiency was derived within these cuts. We note that another method, "cluster counting" [25] is widely used, in particular for "fine grained" TRDs like those used in ATLAS [26] and in HERA-B [27]. As it was shown in [17, 19] and as our own simulations have demonstrated [11], the likelihood on integrated charge gives better pion rejection than the cluster counting method.

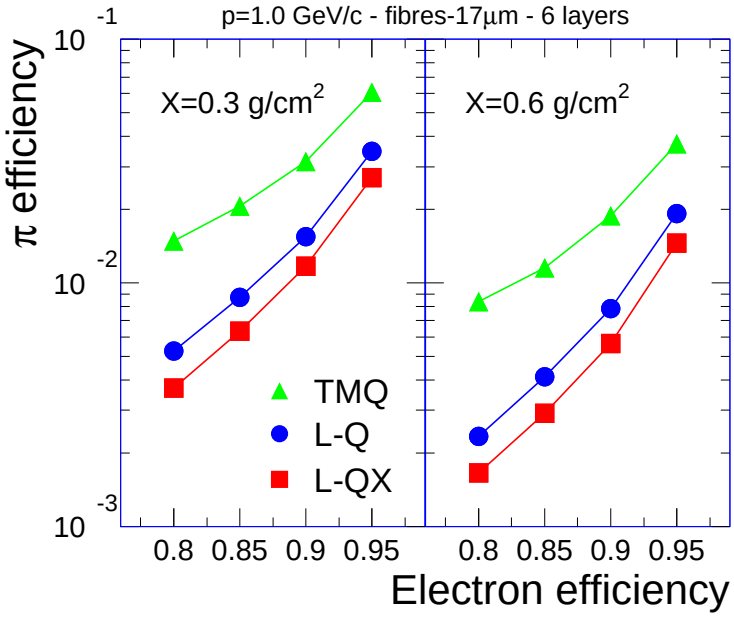

Figure 14.25: Pion efficiency as a function of electron efficiency determined with truncated mean on energy deposit (TMQ), likelihood on total energy deposit (L-Q), two-dimensional likelihood on charge deposit and DC depth (L-QX).

The radiator used for these studies is composed of pure fibres with 17 μm diameter and the detection gas is Xe,CH_4 (10%) . In Fig. 14.25 we present the pion efficiency (the inverse of the rejection factor) as function of electron efficiency (90% electron efficiency is the commonly used value) for the beam momentum of 1 GeV/c. The three methods introduced above are compared. The truncated mean method, although it delivers sizeably worse identification, has the advantage of being very easy to use, being advantageous especially for an on-line identification. The bidimensional likelihood delivers the best rejection factor and will be studied further in order to optimize the final detector design. As emphasized earlier [19], the use of FADCs to process the signals in a TRD can improve the pion rejection power by up to a factor of 2. In general, the three methods employed here give results in good agreement with earlier studies [17, 19].

By doubling the equivalent thickness of the radiator from X=0.3 g/cm^2 (left panel of Fig. 14.25) to X=0.6 g/cm^2 (right panel) one gains a factor of about 2 in pion rejection power. However, as discussed before, it remains to be seen how the additional material will influence the performance of the TRD itself and whether it can be tolerated by other ALICE subdetectors.

The pion efficiency at 90% electron efficiency as a function of momentum is shown in Fig. 14.26. The steep decrease of pion efficiency at momenta around 1 GeV/c is due to the onset of TR production [23, 24]. Towards our highest momentum value, 2 GeV/c, the pion efficiency reaches saturation, determined by the TR yield saturation and by the relativistic rise of the pion. Due to these effects the pion rejection is expected to get slightly worse for momenta above 3 GeV/c [16, 17, 23, 28].

As one can see in Fig. 14.26, at momenta around 2 GeV/c the pion rejection factor of 300 to 500 achieved during these tests is above the required value for the ALICE TRD. However, one has to bear in mind that a significant degradation of TRD performance has been registered when going from prototype tests to real detectors [30]. This is the effect of detector loads in a multiparticle environment, as demonstrated for our case using simulations (see Section 11.5). On the other hand, impressive pion rejection

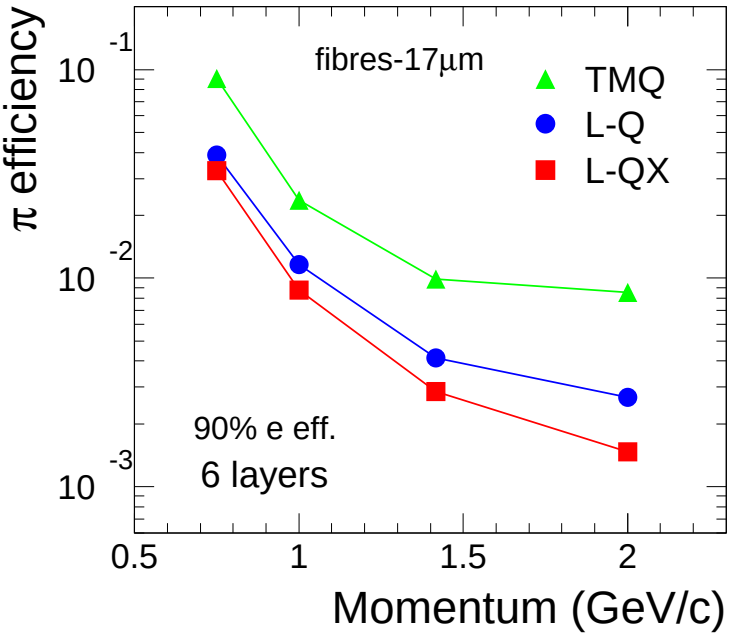

Figure 14.26: Pion efficiency as a function of momentum for a radiator with 17 μm fibres. The three methods used are discussed in the text.

factors of 1000 and above have been achieved in full size TRDs by NOMAD [24] and HERMES [29].

14.3.6 TR performance as a function of incident angle

As shown above (Section 14.3.2), the detector performance depends on the incident angle with respect to the anode wires. Because of the higher energy deposit in case of the electrons (electrons are at the Fermi plateau in the energy loss), they will suffer from stronger gas gain saturation than the pions and this will expectedly affect the pion rejection performance. The radiator used for these studies is the S-HF71 sandwich and the detection gas was Xe,CO_2 (15%) . In Fig. 14.27 we show the electron-pion performance as function of the incident angle. The ratios of pulse heights as a function of the detector depth are shown in the left panel. One can see the expected degradation of these ratios as the incident angle approaches normal incidence. This translates into a degradation of the pion rejection performance, as shown in the right panel. The L-Q method was used to obtain these pion efficiencies extrapolated for 6 layers. The sandwich radiator S-HF71 has been used, for the momentum of 1 GeV/c. The gas gain of the chamber was about 7000.

A higher gas gain obviously contributes to a stronger degradation of the pion rejection performance as seen in Fig. 14.28, where we present the dependence of the pion efficiency at 90% electron efficiency as function of incident angle. Three values of the gas gain are compared, increasing from about 7000 by a factor of 2.35 for each 100 V of the anode voltage. The momentum is 1 GeV/c and the radiator is the sandwich S-HF71. While at the lowest gas gain the degradation in pion rejection is about 30% from 17° to normal incidence, for the higher gains the situation is considerably worse. Almost a factor of four worse pion rejection is observed for the highest gain at normal incidence. One can notice that for incident angles above roughly 10° there is basically no difference in pion rejection for different gains. As discussed above (Section 14.3.2), the gas avalanche is a local process and this explains also the observed dependence of the pion efficiency as a function of angle for different gains (see also related Fig. 14.18).

The degradation of the pion rejection performance as a function of incident angle for high values of the gas gain is an important argument for operating the detectors at the lowest possible gain.

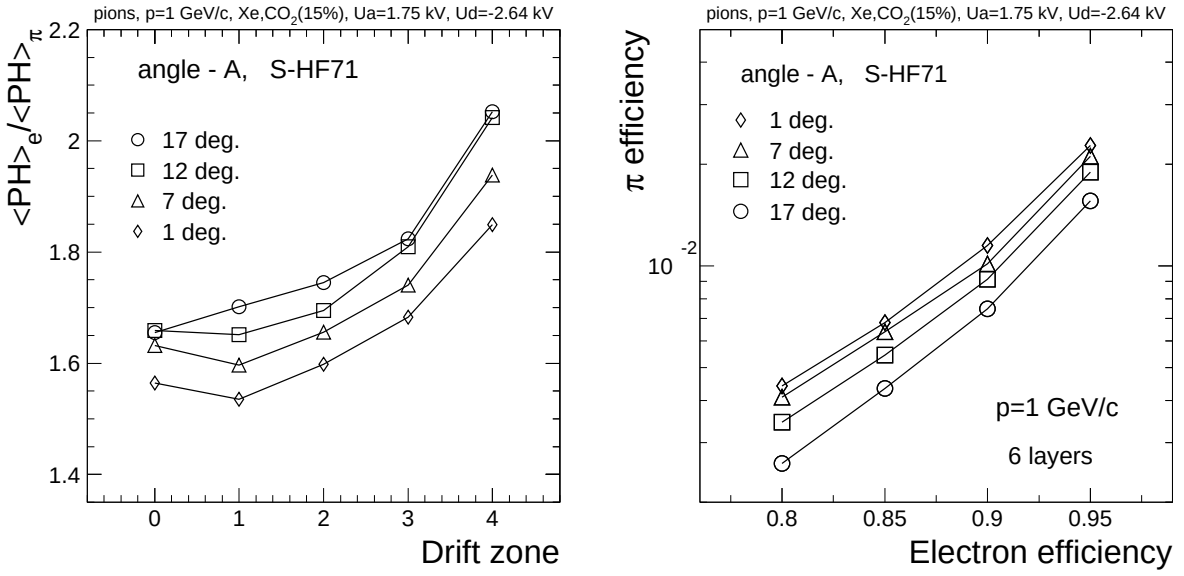

Figure 14.27: Pion rejection performance as a function of incident angle along the anode wires. Left panel: average pulse height ratios; right panel: pion efficiency as a function of electron efficiency. The momentum is 1 GeV/c and the radiator is a sandwich of HF71 foam and 17 μm fibres.

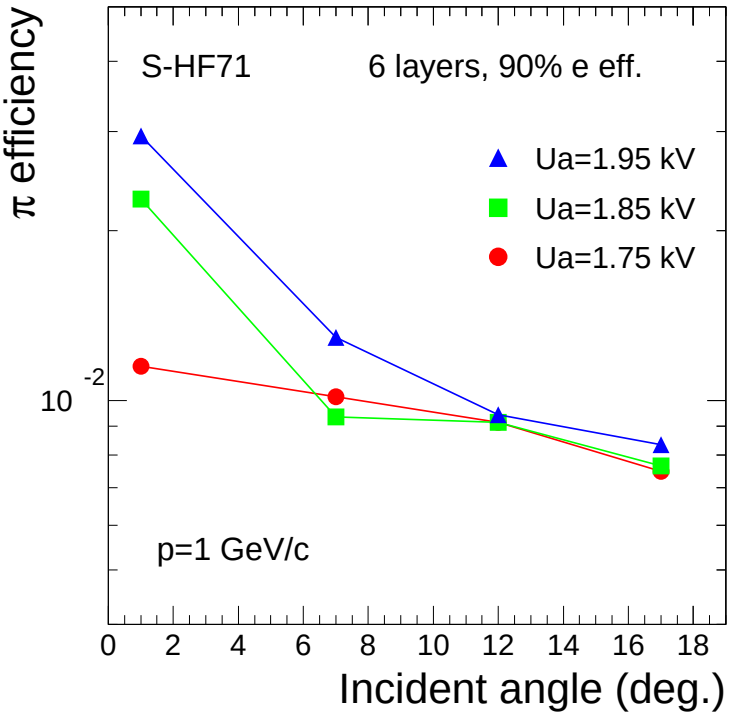

Figure 14.28: Pion rejection performance as a function of incident angle along the anode wires. Three values of the gas gain are compared, increasing by a factor of 2.35 for each 100 V of the anode voltage. The gas mixture is Xe,CO_2 (15%) , Ud=-2.64 kV. The momentum is 1 GeV/c and the radiator is the S-HF71.

14.3.7 Position reconstruction performance

In this section we present results on the position reconstruction performance using a single drift chamber. We study the dependence of the performance on the signal-to-noise ratio for the data without any corrections. Then we justify and apply corrections for the time evolution of the signal and conclude with a study on the influence of a tail cancellation technique, proving its suitability for our data processing chain.

Unless specified, for this study we use 14 time bins of 100 ns each, spanning the full drift region of the DC. Note that there is an uncertainty in assigning the beginning of the drift region (see Fig. 14.13). While this influences the value of the reconstructed angle of incidence, the resolution is changed only marginally. In Fig. 14.29 we present an example of the angle fit. The pulse height distributions over eight pads are presented in the left panel. The fit of the displacement (with respect to the center pad) for each time bin is shown on the right panel. The incident angle was 17° along the anode wires (across pads). It corresponds to a 9.2 mm deflection over the 30 mm drift length.

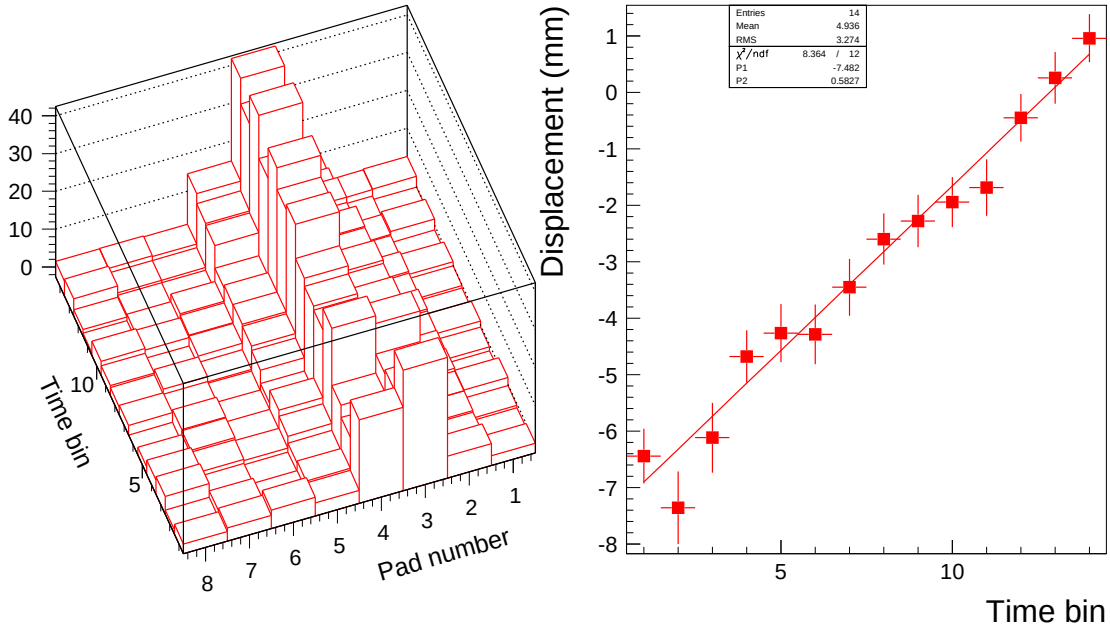

Figure 14.29: Left panel: the pulse height in the drift region versus time bin number on eight pads. Right panel: the displacement from the center pad as a function of time bin number.

In Fig. 14.30 is shown a summary of results as function of signal-to-noise ratio, S/N. The signal is the average pulse height per time bin (for the drift region only) on the center pad, for pions. To vary S/N we increased the gas gain of the detector by varying the anode voltage. The beam incidence was 17° with respect to the normal on the detector, along the anode wires. The upper row presents the average number of pads, $\langle N\,pad\rangle$, with a signal above threshold (cluster width) for each time bin (the threshold was 2 times the noise value) and the average number of points used for the angle fit, $\langle N\,fit\rangle$. We compare three methods for the position reconstruction:

1. the center of gravity using 5 pads, labeled COG5. The displacement from the center of the pad with the maximum signal (pad i) is:

$$x = \frac{-2\cdot P_{i-2} - P_{i-1} + P_{i+1} + 2\cdot P_{i+2}}{P_{i-2} + P_{i-1} + P_i + P_{i+1} + P_{i+2}}, \tag{14.4}$$

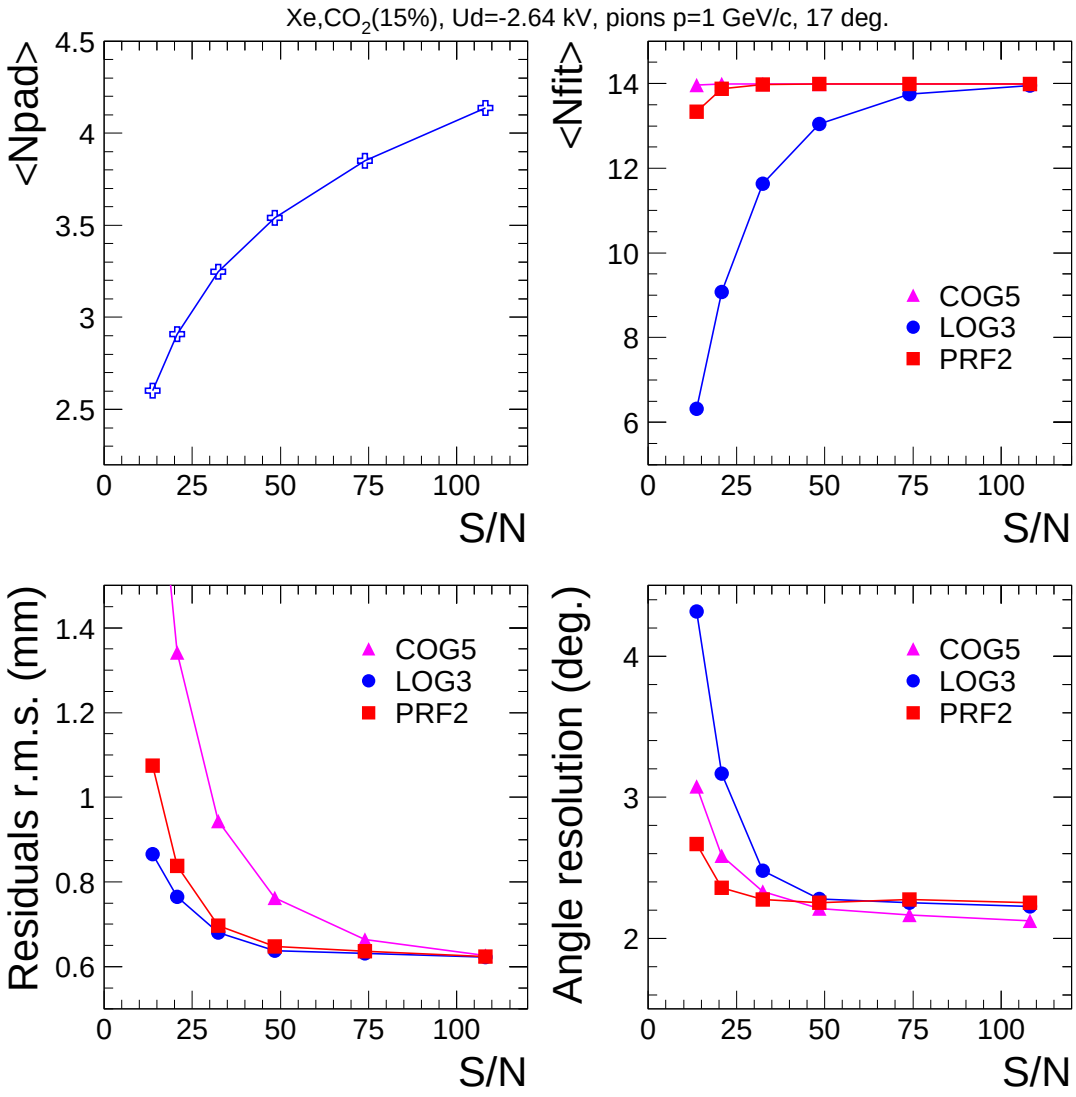

Figure 14.30: The position performance as function of signal-to-noise ratio, S/N. Clockwise from top left: average number of pads with signal over threshold for each time bin, $\langle Npad \rangle$; average number of points used for the angle fit, $\langle N fit \rangle$; angular resolution; r.m.s. of the residuals. The methods used for the position calculation are described in the text.

where P_i is the signal (pulse height for a given time bin) for pad i. The threshold is required only for the central pad.

2. using (for each time bin) formula 14.1, derived under the assumption of a gaussian PRF [5, 6], labeled LOG3. For this method we require that three pads have signals above threshold.

3. an analytical formula using the measured pad response function (see Section 14.2.3), labeled PRF2 [4]. At least two pads are required to be above threshold in this case. In case three pads are above threshold, a weighted mean of two measurements is used [4], so that the displacement for a given

time bin is:

$$x = \frac{1}{w_1 + w_2}\left[w_1\left(\frac{\sigma_P^2}{w}\ln\frac{P_i}{P_{i-1}} - \frac{w}{2}\right) + w_2\left(\frac{\sigma_P^2}{w}\ln\frac{P_{i+1}}{P_i} + \frac{w}{2}\right)\right], \tag{14.5}$$

where σ_P=0.6·w is the known (gaussian) width of the PRF, w=10 mm is the pad width and w_1, w_2 are weights: $w_1 = P_{i-1}^2$, $w_2 = P_{i+1}^2$ [4]. In case the signal in one of the neighbouring pads is below thereshold, this pad is not included in the position calculation. Note that from the beam data using Xe,CO_2 (15%) , we found the PRF to be identical to that measured with Ar,CH_4(10%).

As a consequence of their specific conditions, the three methods have different average number of fit points, as seen in Fig. 14.30 upper right panel.

The lower row in Fig. 14.30 presents the position reconstruction performance: the r.m.s. of the residuals (distance from fit point to the fit value) and the angle resolution (σ of gaussian fit). Here again the three methods show specific behaviour. As expected, as a consequence of different sensitivities to noise for the three methods used, the LOG3 method gives the best resolution at low S/N, while the COG5 method is the worst case. Both the LOG3 and the PRF2 method reach a saturation for S/N>50, while the COG5 method converges to the same resolution only at very high values of S/N. This saturation of resolution as function of S/N indicate the presence of additional sources of errors besides the noise contribution (see below).

Concerning the angular resolution, the three methods differ substantially only at low values of S/N. The poor resolution in case of LOG3 method is a result of the small number of fit points (see upper right panel of Fig. 14.30), while the PRF2 method is a compromise between noise sensitivity and number of fit points. Surprisingly, despite the scatter of the fit points for the COG5 method, leading to sizeably higher values of r.m.s. of residuals, the resolution in angle is only slightly worse than for the PRF2 method at low S/N and even slightly better at large values of S/N.

One can notice from Fig. 14.30 that the angular resolution saturates at lower values of S/N compared to the points resolution (r.m.s. of residuals, which we shall denote as σ_y). This hints to a systematic contribution to the error of the angle that is investigated below. The angle resolution, σ_α, can be written as function of σ_y:

$$\sigma_\alpha \simeq \sqrt{\frac{12}{N_{fit}}}\cdot\frac{\sigma_y}{D} \tag{14.6}$$

where N_{fit} is the number of (independent) fit points and D is the detector depth. For N_{fit}=15 over the drift region D=30 mm, one expects at the limit of high S/N values a limiting resolution of about 1° . The measured values of about 2° are sizeably worse.

The angle determination is sensitive to the Landau fluctuations of the energy deposit along the track. They are biasing the values of the displacement as a function of drift time (and hence the angle) via the asymmetric time response function (TRF) of the detector, due to the ion tail, and of the PASA, due to pole/zero cancellation (see Fig. 14.2, Section 14.2.1). In Fig. 14.31 we give an example of the correlation of the reconstructed angle with the shape of the individual signal. The left panel shows two (extreme) cases, in which the signal is predominantly at the beginning or at the end of the drift time (expressed as time bin number). The arrows mark the drift time position of the average signal, $t_{\langle Q\rangle}$, for each case. The right panel shows, for both cases, the displacement distributions, along with the fits. There is a considerable difference between the two cases: in case of larger clusters at the beginning of the drift (dots) the reconstructed angle is much smaller compared to the case with large clusters later in time (squares). Here and in the following, unless specified, the studies are performed for a moderate value of S/N$\simeq$32.

In Fig. 14.32 we present the correlation of the reconstructed angle with the drift time position of the average signal, $t_{\langle Q\rangle}$ for samples of events in case of pions and electrons. The scale on z is logarithmic. The incidence was 17° with respect to the normal to the anode wires. Pions and electrons show a similar

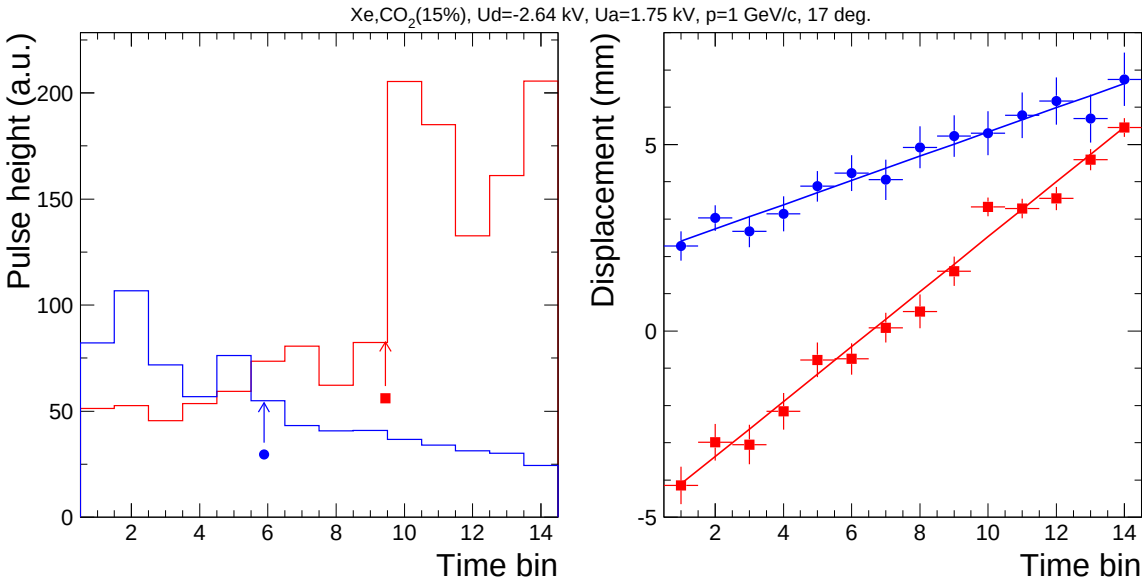

Figure 14.31: Left panel: two examples of the pulse height in the drift region summed up over all pads. Right panel: the displacement from the center pad as a function of time bin number and the result of the fit for the two events of the left panel.

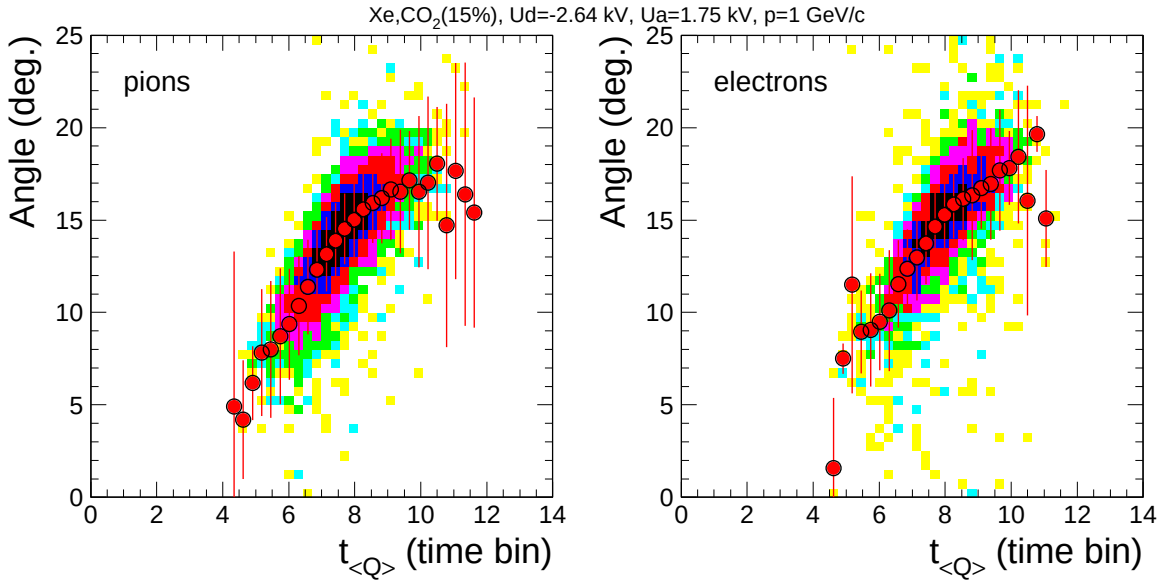

Figure 14.32: The distribution of reconstructed angle vs. the position of the mean charge deposit in the drift time, $t_{\langle Q \rangle}$. The average values are overlayed as dots. The PRF2 method was used for the position reconstruction.

correlation, namely a systematically smaller angle in case of events with large clusters early in time, as illustrated in Fig. 14.31. For higher values of $t_{\langle Q \rangle}$ the reconstructed angle approaches a saturation. The dots in Fig. 14.32 denote the average values of the respective distributions (the errors are the r.m.s.). These values have been used to establish a correction for the angle, taking as reference the largest mea-

sured value (which is actually the true incident angle of 17°). The correction of the angle is done for each track individually, as function of $t_{\langle Q \rangle}$. The correction is the same for electrons and pions.

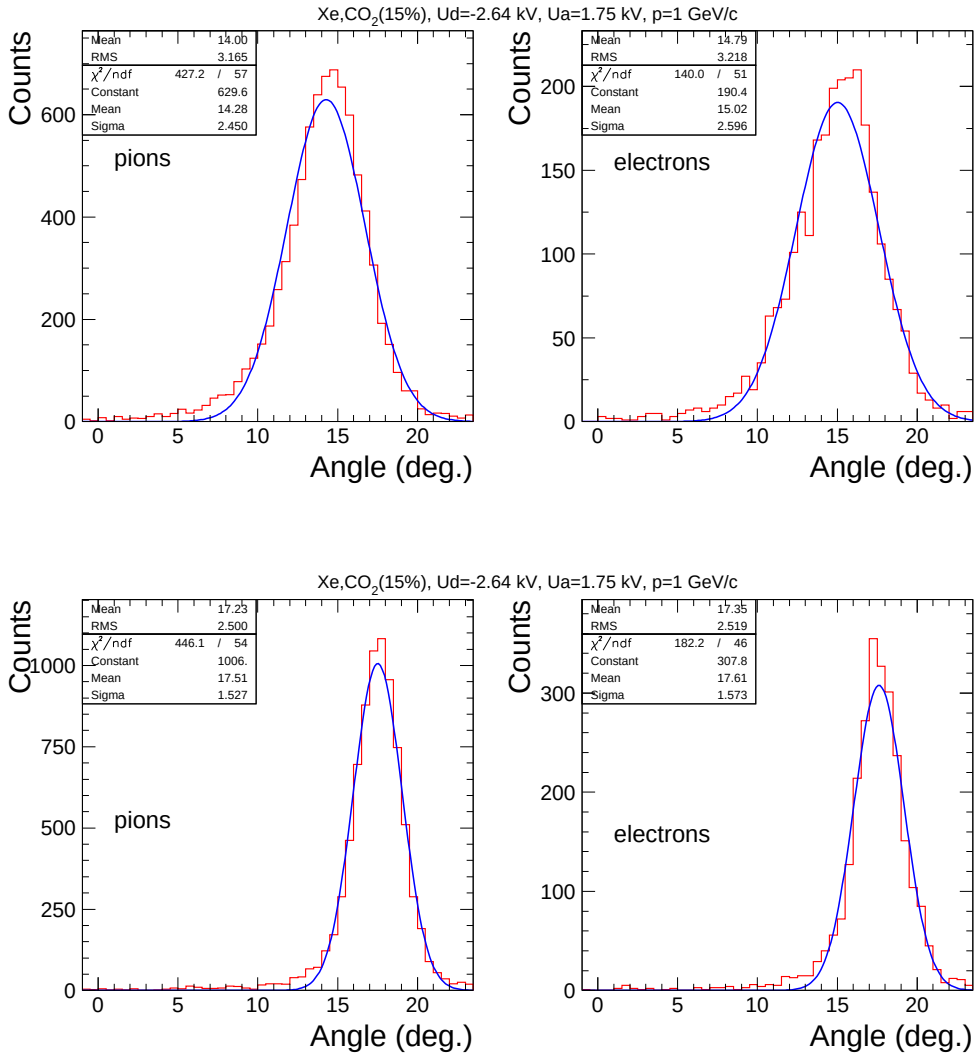

Figure 14.33: Angle reconstruction performance for pions and electrons, before (upper row) and after (lower row) the correction for the mean charge deposit. The PRF2 method was used for the position reconstruction and the incident angle was 17° .

Figure 14.33 presents the distributions of the reconstructed angles for both pions and electrons, before (upper row) and after (lower row) the correction for the mean charge deposit. The thicker curves are the result of gaussian fits. A clear improvement of the angular resolution, by about 1° , is seen as a result of the correction. Obviously, the centroid of the angle distribution is also affected by the correction.

A summary of the effect of the above correction as a function of the incident angle is presented in Fig. 14.34 for both pions and electrons. The correction was determined separately for each angle. Notice that not only the resolution is worse prior to the correction, but also the reconstructed angle is smaller than the real angle by several degrees. The correction restores the original angle and improves the resolution, as seen already in Fig. 14.33. The correction is less significant for smaller incident angles, with no effect at normal incidence (in fact, at normal incidence there is no correlation of angle vs. $t_{\langle Q \rangle}$).

We turn now to a more detailed study of the position and angular resolution as a function of the

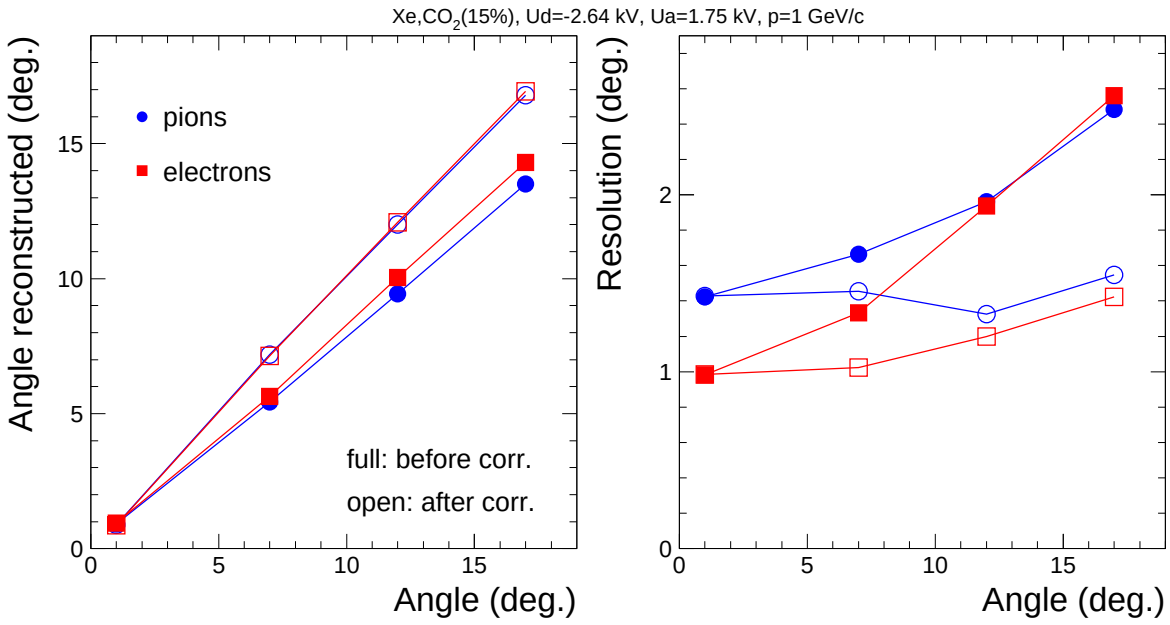

Figure 14.34: Angle reconstruction performance for pions and electrons, as a function of the incident angle, before (full symbols) and after (open symbols) the correction. The PRF2 method was used for the position reconstruction.

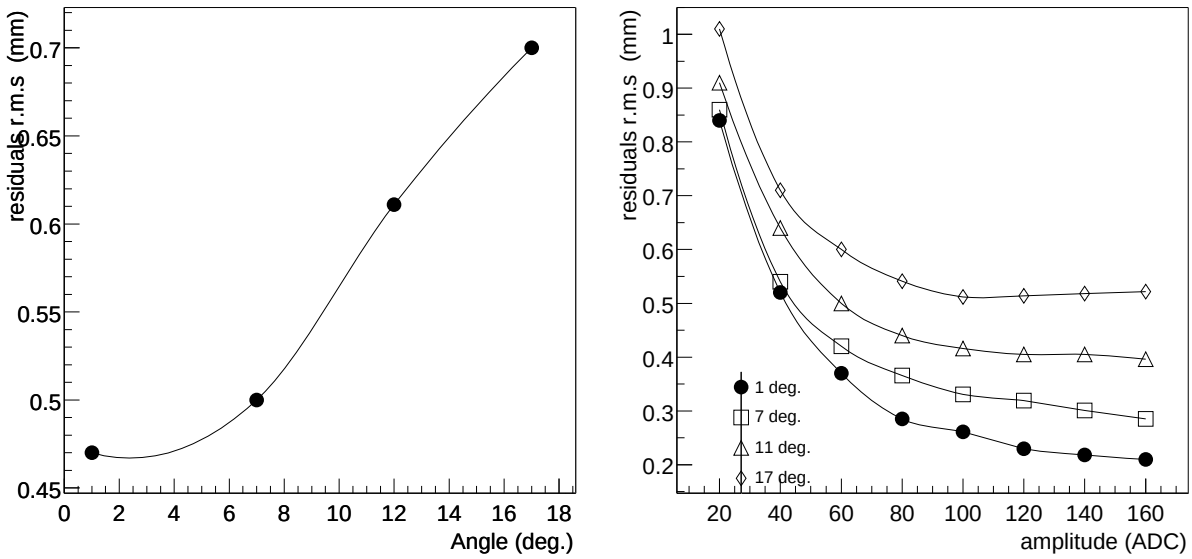

Figure 14.35: Left panel: r.m.s. of residuals as a function of incident angle. Right panel: r.m.s. of residuals as a function of signal magnitude for different incident angles.

incident angle. In Fig. 14.35 we show a summary of the position resolution (r.m.s. of the residuals) as function of the incident angle. The left panel shows the resolution as a function of incident angle, while the right panel presents a differential view of the resolution, namely its variation as a function of the amplitude (the sum of the signal over the pad cluster in each time bin) for the four incident angles. The noise level is about 1.2 ADC channels. In the limit of large signals, resolutions down to 200 μm

are achieved for normal incidence. Also in this representation, the resolution exhibits a saturation as a function of the signal magnitude, however, the saturation is reached for higher values of S/N and for lower values of the resolution as compared to the integral values presented in Fig. 14.30. Notice also the different amplitude dependence in the approach to saturation as a function of the incident angle. Here and for the following results a look-up table method (LUT) based on the known PRF was used for the position reconstruction. It gives results comparable to the PRF2 method presented above and has the advantage that it is easy to use for position calculations at the trigger level (see Chapter 6).

Despite the fact that the correction of the angles due to Landau fluctuations is quite effective, a more natural approach is the so-called "tail cancellation", namely subtracting the known signal tail as a function of time. It can be done either at the level of the analog electronics, as it was originally proposed, using a pole/zero network [31] or at the level of the digitized signal by employing a digital filter [32]. In either case, the operations are the equivalent of de-convoluting the signal with the following transfer function [31]:

$$f(s) = \frac{s + 1/\tau}{s + k/\tau} \tag{14.7}$$

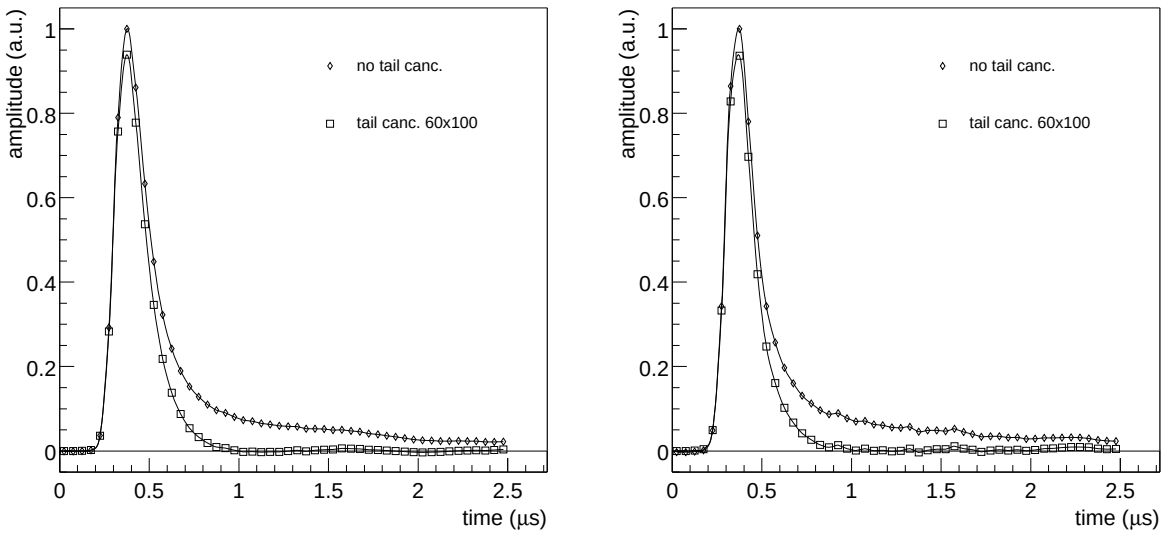

Figure 14.36: Average signals for ^{55}Fe source on center (left panel) and neighbouring pad (right panel), before (diamond symbols) and after the tail cancellation (squares).

We applied such a deconvolution for the measured data in the off-line data analysis. Fig. 14.36 shows average signals from the ^{55}Fe source on the center pad (left panel) and on a neighbouring pad (right panel) before and after the deconvolution with the function 14.7. One can see that the long tail is cancelled quite accurately for the chosen set of parameters ($k \times \tau$, where τ is expressed in time bins of 10 ns each). The values τ=1.0 μs, k=1.67 were found to provide the optimum angular resolution and are used in the following studies.

In Fig. 14.37 we present an example of the average pulse height as function of drift time for pions, before (left panel) and after (right panel) the tail cancellation. Two effects of the cancellation are seen: i) the originally slightly rising plateau (left panel) is made perfectly flat (right panel); ii) the average signal in the drift region is reduced by about 37%, as can be seen from the fits of the plateau regions (thick straight lines); this implies the necessity to work at higher gas gain in order to compensate for the signal loss.

In Fig. 14.38 we compare the angular resolution for the original data (upper left panel), after the $t_{\langle Q \rangle}$ correction (upper right panel) and after the tail cancellation algorithm (lower panel). For this investigation

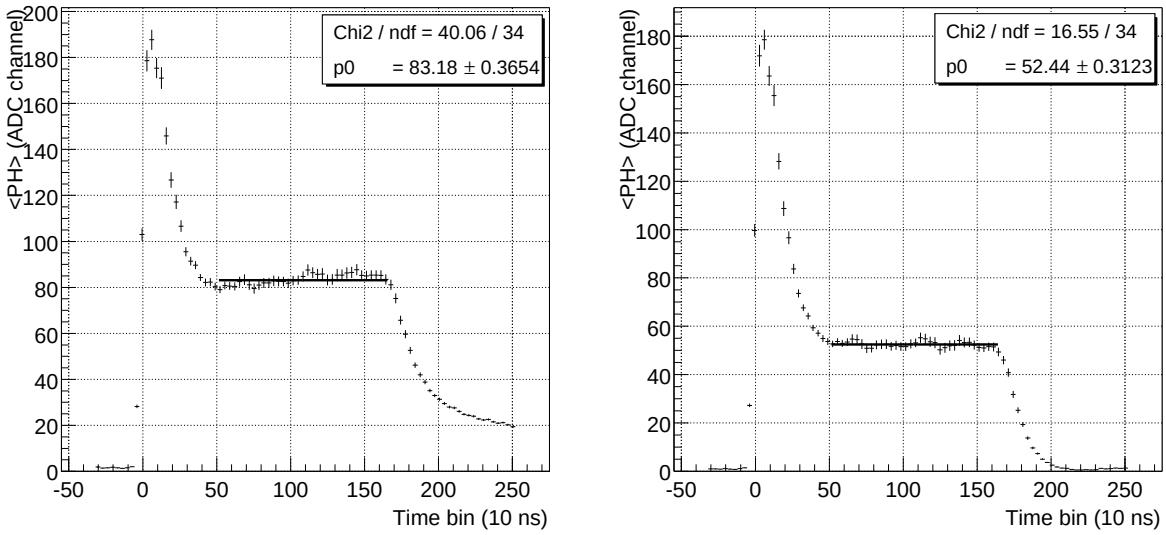

Figure 14.37: Average pulse height as function of drift time for pions, before (left panel) and after (right panel) the tail cancellation.

the amplification region was included in the angle fit, amounting to additional 3 time bins of 100 ns each. Despite the fact that the drift velocity is not constant in the amplification region, clean clusters contribute there to a better angle resolution for the uncorrected data, compared to the case when only the drift region was used (see previous Fig. 14.35 and below). Different methods of data analysis are compared in Fig. 14.38: i) 17 points (time samples of 100 ns each) are used for the fit (this is closest to the configuration of the final detector); ii) 33 samples of 50 ns are fitted; iii) 160 samples of 10 ns (our highest sampling resolution) each are used; iv) 160 samples are used, but the fit points are weighted by ther individual pulse heights. For the last two cases in addition a cut on the cluster width (in the pad direction) is used, to minimize the contribution of δ-rays. The different ways of analysis show little differences in case of both uncorrected and $t_{\langle Q \rangle}$-corrected cases, but in case of the tail cancellation analysis, as expected, a finer time sampling clearly leads to a better angle resolution. Overall, the tail cancellation leads to angular resolutions below 1° for all the incident angles, sizeably better compared to the $t_{\langle Q \rangle}$ correction. Note that at the lowest incident angle the tail cancellation amounts to a small degradation of the angle resolution, mainly as a result of the degradation of the S/N ratio.

In Fig. 14.39 we summarize the S/N dependence of the position (left panel) and angle (right panel) resolution for 17° incidence, using various corrections. The uncorrected data (crosses) are compared to the values after the $t_{\langle Q \rangle}$ correction (dots) and after the tail cancellation (squares) for 14 fit points in the drift region. Obviously, the $t_{\langle Q \rangle}$ correction does not affect the point resolution (the dots are overlapping the crosses), but acts only on the angular resolution. Conversely, the tail cancellation is affecting the point resolution as well and this translates into a better angular resolution. The triangles indicate the tail cancellation method for the case of including the amplification region into the fit. For this last case the S/N value is improved for a given gas gain. However, for the same value of S/N, the point resolution suffers a degradation, presumably as a result of non-constant drift velocity in the amplification region. This is reflected in the angular resolution, where the improvement is less than expected from the scaling to the number of fit points (a factor of 1.16 improvement compared to the ratio 17/14=1.21). One can notice that the approach towards saturation for increasing S/N is different for the various cases presented, essentially the corrected values having a more accentuated dependence of S/N, as expected after essentially removing the systematic (dominant) contributions.

Finally, in Fig. 14.40 we show the distribution of the time of the first electron arrival, t_{first}, as a function of the position across the anode wires, y, measured with the Si-strip detectors. The 5 mm

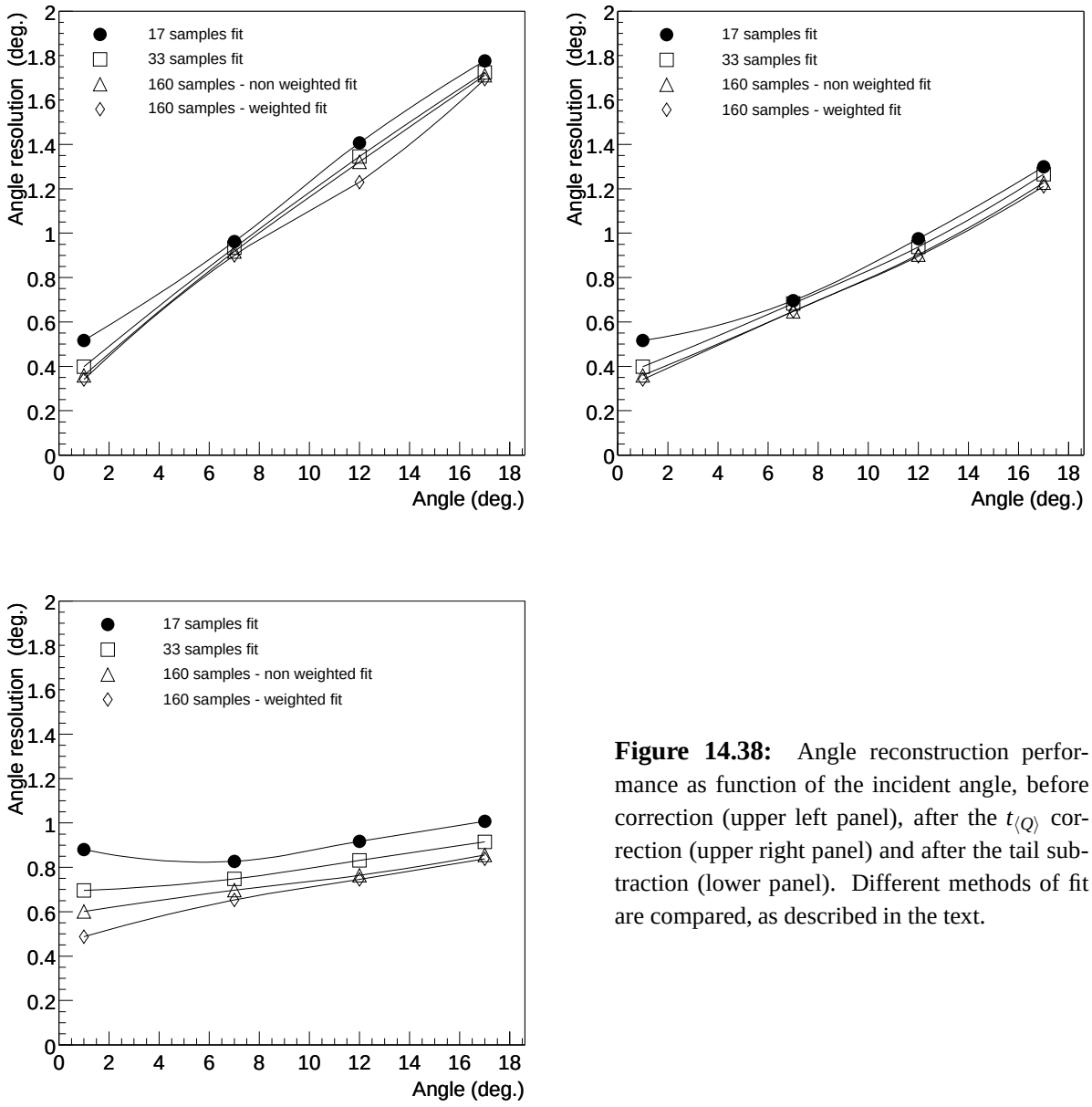

Figure 14.38: Angle reconstruction performance as function of the incident angle, before correction (upper left panel), after the $t_{\langle Q \rangle}$ correction (upper right panel) and after the tail subtraction (lower panel). Different methods of fit are compared, as described in the text.

periodicity reflects the wire pitch. The variation of the arrival time within one drift cell is the result of the isochronity variation due to the field configuration. When exploited in a pad geometry staggered across the anode wires (in the real detector z direction, along the beam), the information on t_{first} can provide a position accuracy much better than the wire pitch. This feature can be an important constraint for the TPC tracking and may also be used for its absolute drift calibration.

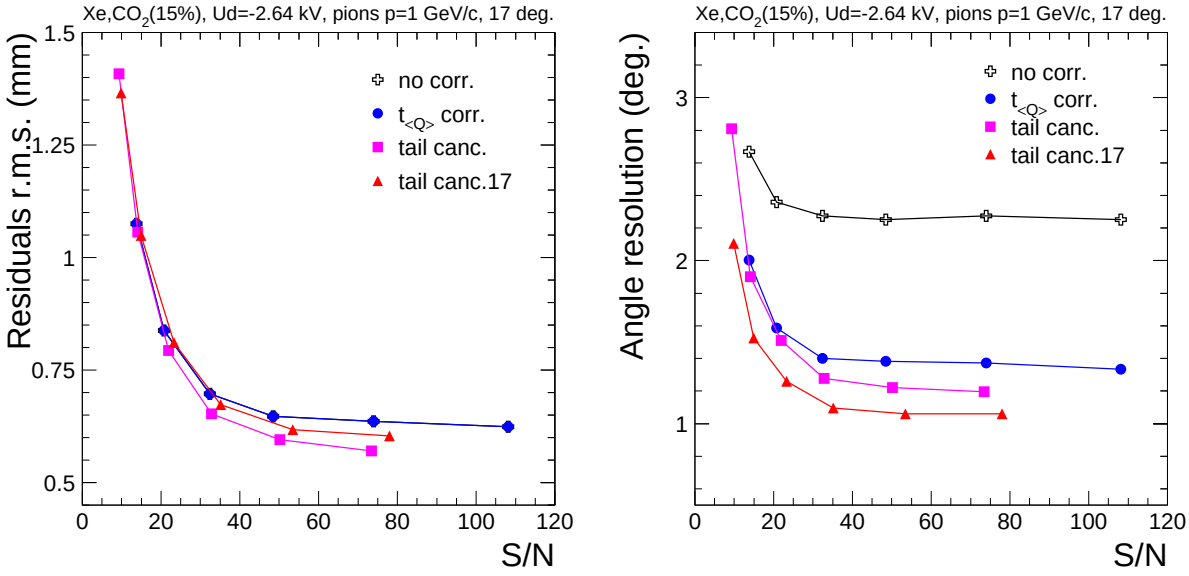

Figure 14.39: Position (left panel) and angular (right panel) resolution as a function of S/N for data without correction (crosses), after the $t_{\langle Q \rangle}$ correction (dots) and after the tail cancellation (squares) for 14 fit points in the drift region. The triangles denote the tail cancellation method, but including the amplification region into the fit.

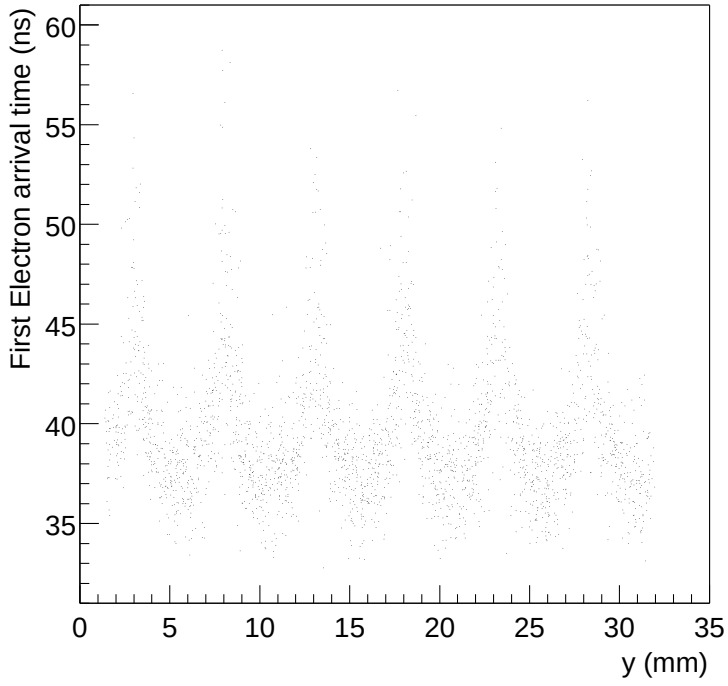

Figure 14.40: The distribution of the time of the first electron arrival as a function of the coordinate across the wires, measured by the Si-strip detectors.

14.4 Work in progress

New prototypes were recently built with pads both of chevron type (w=10 mm, l=60 mm) and rectangular (w=7.5 mm, l=80 mm). To have a similar pad response function, the anode-cathode gap (h) is 2.5 mm in case of chevron pads and 3.5 mm for the rectangles. The anode wire diameter is 20 μm. To facilitate a fast exchange of different pad planes on the same detector body, these new prototypes have smaller dimensions: 25×31 cm^2. Two wire configurations for the cathode plane were realized, with 5 mm and 2.5 mm wire pitch. In both cases we used a staggered geometry (see Chapter 4). Photographs of both the chevron (left panel) and rectangle (right panel) pad planes are shown in Fig. 14.41. These prototypes were tested with an ^{55}Fe source and in beam at GSI in August 2001. We present here the detailed measurements with the ^{55}Fe source and some results from the beam measurements.

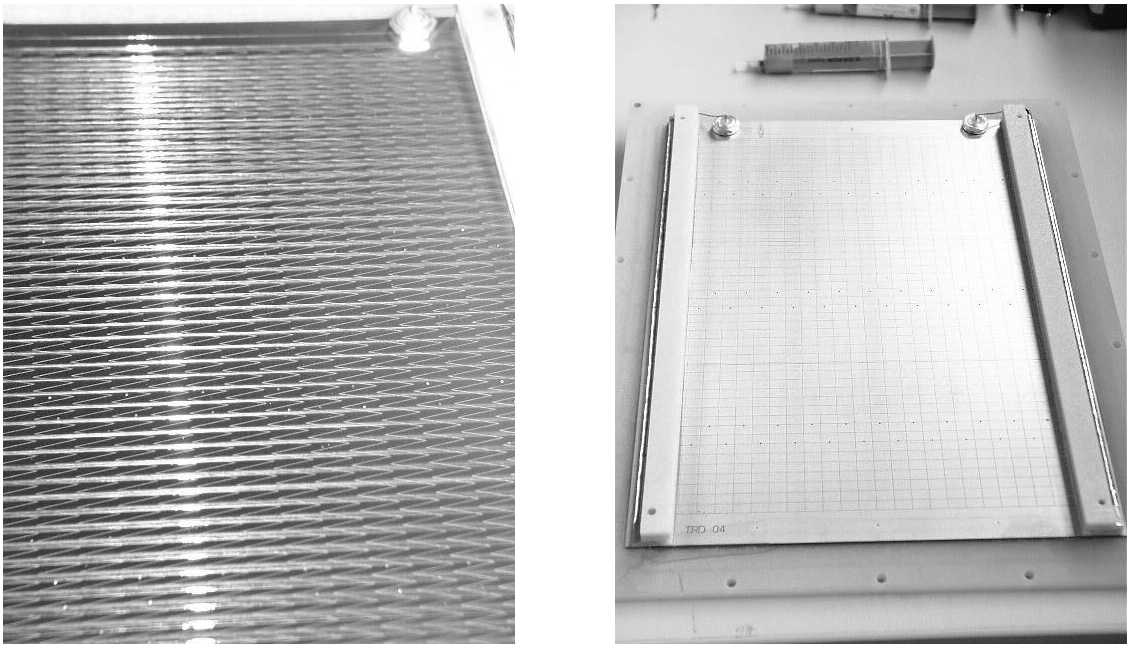

Figure 14.41: Photographs of the pad planes with chevron type (left panel) and rectangular (right panel) pads.

In Fig. 14.42 we present the gain curves: the average pulse height for the main peak of the ^{55}Fe source as function of the anode voltage. Roughly 100 V higher anode voltage is necessary in order to achieve the same gas gain for the h=3.5 mm configuration (rectangles), compared to the h=2.5 mm case (dots). This is slightly less than the difference predicted by GARFIELD [12] calculations (Section 4.6, Fig. 4.17).

Note that comparable values of the pulse height are obtained for lower voltages compared to the first prototype (see Fig. 14.6 in Section 14.2.2). The interpolation of the case h=3.0 mm of the first prototype leads us to conclude that roughly 150 V less are needed for the same gas gain when changing the anode wire diameter from 25 to 20 μm. In case of the denser cathode wire grid, with wire pitch of 2.5 mm (open symbols in Fig. 14.42), the gas gain is slightly higher for the same anode voltage, as a result of a better confined amplification region.

In Fig. 14.43 we present the dependence of the ^{55}Fe pulse height on the drift voltage. As a result of the drift field penetrating the cathode wire grid, the gas gain is increasing as function of the drift voltage. It is evident that the magnitude of this effect is different for the two cathode wire configurations. At fixed anode voltage, in case of 5 mm cathode pitch (full symbols) the gas gain increases by almost 60% for an increase of 1.5 kV in drift voltage. For 2.5 mm pitch (open symbols) the increase is only 26%. The two cases of anode-cathode gap show similar dependence of the gas gain as a function of the drift voltage. Apparently, the difference on gain between the two configurations (at fixed drift voltage) is higher for the 2.5 mm cathode wire pitch, as seen also in Fig. 14.42.

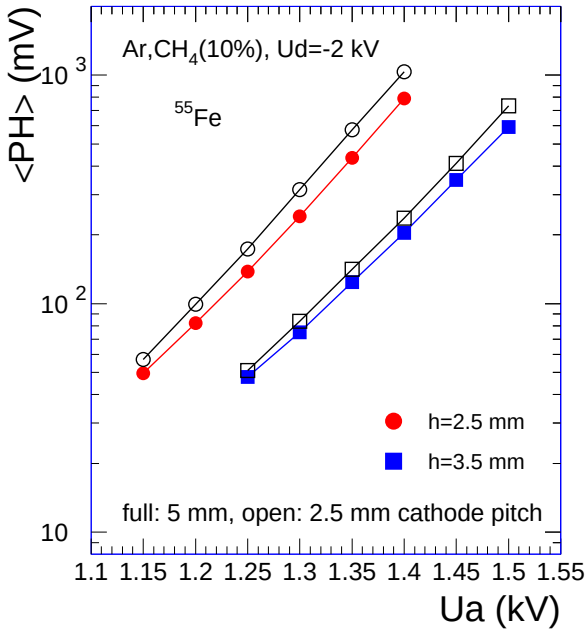

Figure 14.42: Pulse height of ^{55}Fe as a function of the anode voltage for two cases of anode-cathode gap, for cathode wire pitch of 5 mm (full symbols) and 2.5 mm (open symbols).

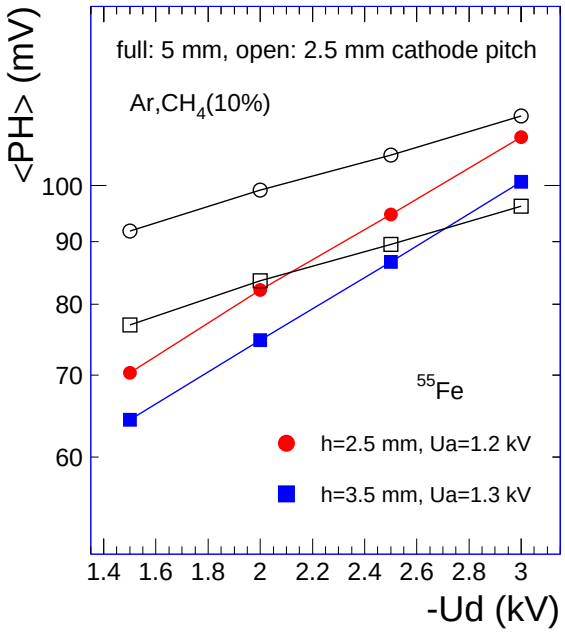

Figure 14.43: Pulse height of ^{55}Fe as a function of the drift voltage for cathode wire pitch of 5 mm (full symbols) and 2.5 mm (open symbols) for two cases of anode-cathode gap.

In Fig. 14.44 are shown the PRFs for the chevron (left panel) and the rectangle (right panel) pad planes. We compare the 5 mm and 2.5 mm cathode wire pitch and conclude that the cathode grid density influences only marginally the PRFs. As seen already in Section 14.2.3 (Fig. 14.7), the calculated values do not agree with the measured ones. This disagreement is similar for chevron and rectangle pad planes and is being investigated further.

During the beam measurements in August 2001 we have performed the following:

- a relative comparison of the position reconstruction performance of the chevron and rectangular pads.
- a study of sandwich radiators reinforced with carbon or glass fibre.
- a study of the drift chambers performance as a function of the oxygen content in the detection gas.
- we placed the detectors in a magnetic field of up to 0.3 T, with the aim to measure Lorentz angles and to compare the position resolution with and without magnetic field.

While the bulk of the data evaluation is in progress, we present here the results on the study of the chamber performance under oxygen contamination. In Fig. 14.45 we show the average pulse height distributions as a function of drift time (left panel) and the pion efficiency as a function of electron efficiency for different values of the oxygen content in the range of a few hundred ppm. From the measurements of the pulse height distributions as a function of drift time we deduced an attachment coefficient C_{att}=400 atm$^{-2}\mu$s^{-1} (see Chapter 4). As seen in the right panel of Fig. 14.45, the pion rejection performance is slightly degrading for increasing oxygen contamination. This is one argument to keep the oxygen at the lowest possible value.

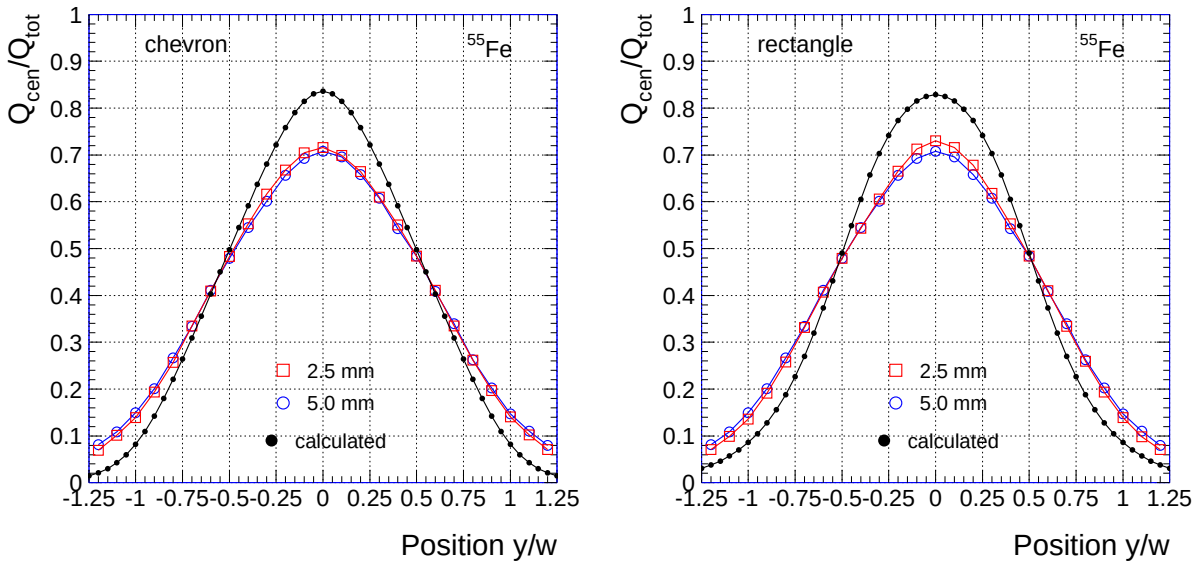

Figure 14.44: Pad response functions for chevron (left panel) and rectangle (right panel) pad planes. The 5 mm (circles) and 2.5 mm (rectangles) cathode pitch are compared.

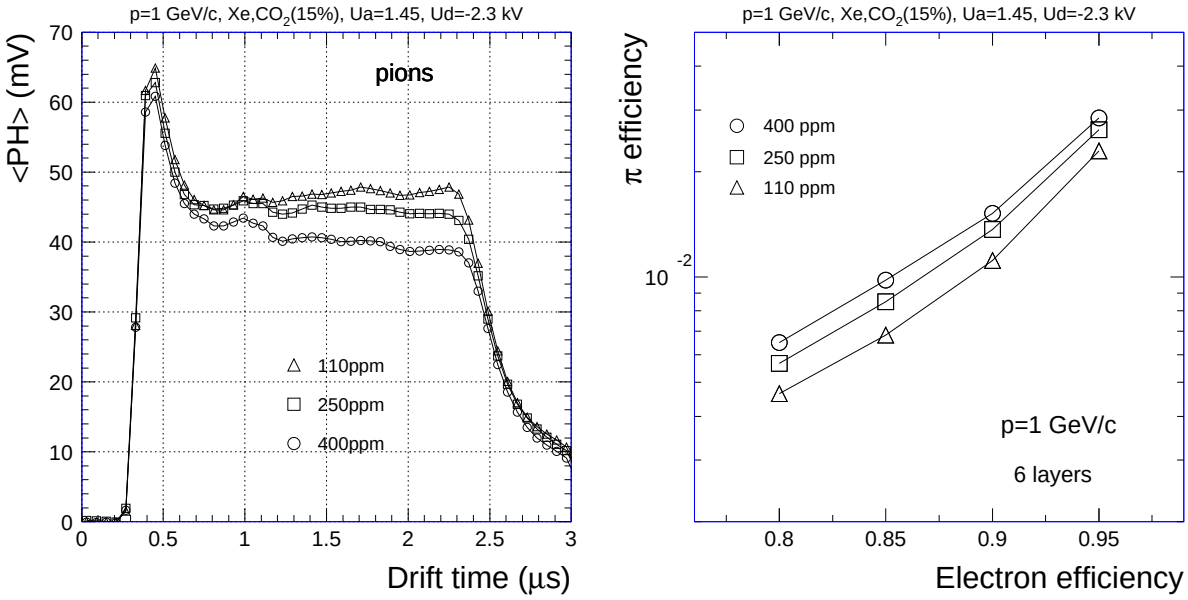

Figure 14.45: Drift chamber performance as a function of oxygen content. Left panel: average pulse height distributions as a function of drift time. Right panel: pion efficiency as a function of electron efficiency.

Apart from the analysis of newly measured data, ongoing work include on-detector implementation of the integrated electronics and preparations for beam tests at CERN, where in particular the TR performance for momenta above 2 GeV/c will be measured. These measurements are scheduled for October-November 2001.